American Mineralogist, Volume 82, pages 1150–1175, 1997

Structural mechanism of Co^{2+} oxidation by the phyllomanganate buserite

Alain Manceau,[1,*] Victor A. Drits,[2] Ewen Silvester,[1,†] Céline Bartoli,[1] and Bruno Lanson[1]

[1]Environmental Geochemistry Group, LGIT-IRIGM, University of Grenoble and CNRS, 38041 Grenoble Cedex 9, France
[2]Geological Institute of the Russian Academy of Sciences, 7 Pyzhevsky street, 109017 Moscow, Russia

Abstract

The geochemistry of Co at the Earth's surface is closely associated with that of manganese oxides. This geochemical association results from the oxidation of highly soluble Co^{2+} to weakly soluble Co^{3+} species, coupled with the reduction of Mn^{4+} or Mn^{3+} ions, initially present in the manganese oxide sorbent, to soluble Mn^{2+}. The structural mechanism of this Co immobilization-manganese oxide dissolution reaction was investigated at the buserite surface. Co-sorbed samples were prepared at different surface coverages by equilibrating a Na-exchanged buserite suspension in the presence of aqueous Co^{2+} at pH 4. The structure of Co-sorbed birnessite obtained by drying buserite samples was determined by X-ray diffraction (XRD) and powder and polarized EXAFS spectroscopy. For each sample we determined the proportion of interlayer cations and layer vacancy sites, the $Co^{2+}/(Co^{2+} + Co^{3+})$ ratio, the nature of Co sorption crystallographic sites, and the proportion of interlayer vs. layer Co. From this in-depth structural characterization two distinct oxidation mechanisms were identified that occur concurrently with the transformation of low pH monoclinic buserite to hexagonal H-rich birnessite (Drits et al. 1997; Silvester et al. 1997). The first mechanism is associated with the fast disproportionation of layer Mn^{3+} according to $2Mn^{3+}_{layer} \rightarrow Mn^{4+}_{layer} + \square_{layer} + Mn^{2+}_{solution}$, where $\square$ denotes a vacant site. Divalent Co sorbs above or below a vacant site ($\square_1$) and is then oxidized by the nearest Mn^{3+}_{layer}. The resulting Co^{3+} species fills the $\square_1$ position while the reduced Mn migrates to the interlayer or into solution creating a new vacant site ($\square_2$). This reaction can be written: $Co^{2+}_{solution} + \square_1 + Mn^{3+}_{layer} \rightarrow Co^{2+}_{interlayer} + \square_1 + Mn^{3+}_{layer} \rightarrow Co^{3+}_{interlayer} + \square_1 + Mn^{2+}_{layer} \rightarrow Co^{3+}_{layer} + \square_2 + Mn^{2+}_{sol/inter}$. This mechanism may replicate along a Mn^{3+}-rich row, and, because the density of vacancies remains constant, it can result in relatively high Co concentrations, as well as domains rich in Co^{3+}_{layer}-Mn^{4+}_{layer}. During the low-pH buserite transformation, about one-half of the layer Mn^{3+} that does not disproportionate migrates from the layer to the interlayer space creating new vacancies, with the displaced Mn^{3+} residing above or below these vacancies. The second oxidation mechanism involves the replacement of $Mn^{3+}_{interlayer}$ by $Co^{3+}_{interlayer}$; the latter may eventually migrate into layer vacancies depending on the chemical composition of octahedra surrounding the vacancy. The criterion for the migration of Co^{3+} into layer vacancies is the need to avoid Mn^{3+}_{layer}-Co^{3+}_{layer}-Mn^{3+}_{layer} sequences. The suite of chemical reactions for this second mechanism can be schematically written: $Co^{2+}_{solution} + Mn^{3+}_{interlayer} + \square \rightarrow Mn^{2+}_{solution} + Co^{3+}_{interlayer} + \square \rightarrow Mn^{2+}_{solution} + Co^{3+}_{layer}$, the last step being conditional. In contrast to the first mechanism, this second mechanism decreases the density of vacant sites. At high surface coverage, Co-sorbed birnessite contains a substantial amount of unoxidized $Co^{2+}_{interlayer}$ species despite some non-reduced Mn^{3+} in the sorbent. This result can be explained by the sorption of $Co^{2+}_{solution}$ onto vacant sites located in Co^{3+}_{layer}- and Mn^{4+}_{layer}-rich domains devoid of Mn^{3+}. The number and size of these domains increase with the extent of oxidation and the total Co concentration in the solution, and this accounts for the decreasing capacity of buserite to oxidize Co. The weight of structural evidence indicates that Co is oxidized by Mn^{3+} rather than Mn^{4+}. Thermodynamic considerations indicate that under the solution pH conditions employed in this study Mn^{3+} is the more likely electron sink for the oxidation of Co^{2+}. This study also shows that the high affinity of Co for man-

* Alain.Manceau@obs.ujf-grenoble.fr
† Present address: CSIRO, Division of Minerals, Box 312, Clayton South Victoria, Australia, 3169.

0003–004X/97/1112–1150$05.00

ganese oxides is not only due to its oxidation to weakly soluble Co^{3+} species, but also because of the reducted layer strains from the substitution of Co^{3+} for Mn^{3+}.

Results obtained for these model compounds were compared with those for natural Co-containing asbolane and lithiophorite (Manceau et al. 1987). This comparison indicates that the different structural mechanisms explored in the laboratory can satisfactorily account for the observations made on natural samples. Specifically, the present study proves that Co substitutes for Mn in natural phyllomanganates and allows us to eliminate the possibility of precipitation of discrete CoOOH particles.

INTRODUCTION

It has long been recognized that manganese oxides exhibit strong control on the environmental distribution of Co. Early observations by Taylor and coworkers (Taylor 1968; Taylor and McKenzie 1966; Taylor et al. 1964) showed that manganese minerals lithiophorite, hollandite, and birnessite (dehydrated form of buserite) present in Australian soils contain relatively large amounts of Co. This geochemical Mn-Co association was also recognized in deep-sea nodules and crusts (Burns and Burns 1977). In addition, monomineralic Co-containing Mn phases, such as asbolane and lithiophorite, have been identified in oceanic nodules, soils, and lateritic formations (Chukhrov et al. 1982; Chukhrov et al. 1980; Llorca 1987; Manceau et al. 1987; Ostwald 1984). Many laboratory experiments have been performed to understand the reason for this unusually high geochemical selectivity of manganese oxides for Co (Balistrieri and Murray 1986; Gray and Malati 1979; Loganathan and Burau 1973; McKenzie 1967; Means et al. 1978; Murray 1975). In general, sorbed Co is strongly bound and sparingly extractable. Its sorption is accompanied by a release of Mn^{2+} and a darkening of the manganese oxide. These facts were attributed to an electron transfer between sorbed Co^{2+} and manganese oxide (McKenzie 1970; McKenzie 1980; Traina and Doner 1985). Direct evidence for the oxidation of Co^{2+} to Co^{3+} at the surface of manganese oxides was first reported by Murray and Dillard (1979) using X-ray photoelectron spectroscopy (XPS), and this technique was then used to demonstrate the trivalent state of Co in oceanic nodules (Dillard et al. 1982). More recently, Manceau et al. (1987) showed by extended X-ray absorption fine structure spectroscopy (EXAFS) that Co is trivalent and in a low spin electronic configuration (d^6) in lithiophorite and asbolane from a New Caledonian soil. Although the oxidation state of Co in Mn-rich natural samples is now well established, the mechanism of its oxidation at the atomic scale and the structural reasons for its immobilization remain poorly understood. Dillard et al. (1982) showed that Co^{2+} is oxidized by Mn^{3+} or Mn^{4+} at the surface of the phyllomanganate birnessite and that XPS spectra of Co-sorbed complexes were consistent with Co^{3+} in an oxide or hydroxide environment such as CoOOH or $Co(OH)_3$. EXAFS Co-(O,OH) and Co-(Co,Mn) interatomic distances were found to be identical to those of Mn atoms in Co-containing lithiophorite and asbolane. This result indicates that Co atoms are present in a layered, phyllomanganate-type structure. The structural environment of Co and Mn atoms strongly differed, however, by their short range ordering: The amplitudes of Co-EXAFS spectra and radial structure functions (Co-RSF) were systematically enhanced compared to Mn-EXAFS and Mn-RSF. The origin of this difference in local order is still a mystery. These experiments allowed a random distribution of Co atoms in Mn layers to be ruled out, and Co was inferred to be segregated in Co-rich domains, either dispersed in phyllomanganate layers or forming individualized CoOOH layers (Manceau et al. 1987).

The work presented in this paper was undertaken to gain further insight into the crystal chemistry of Co in phyllomanganate structures. The main challenge in studying this system originates from the fact that Mn^{4+} and low-spin Co^{3+} ions have practically the same ionic radius (0.53 Å and 0.54 Å, respectively) and atomic number, preventing them from being formally distinguished by electron and X-ray diffraction. To reach our objective, three factors proved to be critical. First, the phyllomanganate buserite was used as the sorbent in aqueous solution. This mineral is a powerful oxidant and has often been used for studying surface redox reactions (Bidoglio et al. 1993; Fendorf and Zasoski 1992; Fendorf et al. 1993; Manceau and Charlet 1992; Oscarson et al. 1983; Silvester et al. 1995; Stone and Morgan 1984; Stone and Ulrich 1989). The poor knowledge of the defective nature of solids belonging to the buserite and birnessite group (Strobel et al. 1987) was the principal limitation to understanding these reactions at the atomic level. This limitation has now been overcome with the recent structural studies by Drits et al. (1997) and Silvester et al. (1997), who have determined the spatial distribution of lower valence Mn (Mn^{3+} and Mn^{2+}) and the density and distribution of layer cation vacancies. Second, Co-sorbed birnessite samples were prepared at different surface coverages so that birnessites with varying Co^{2+}/Co^{3+} ratios were produced. As shown later, the simultaneous presence of Co^{2+} and Co^{3+} in some samples has proved very helpful in gaining an understanding of the early steps in the oxidation mechanism. Third, quantitative powder X-ray diffraction (XRD) as well as powder and polarized EXAFS methods were used as complementary techniques. The unique combination of these three factors proved to be critical in solving many aspects of the crystal chemical properties of the Co-phyllomanganate system.

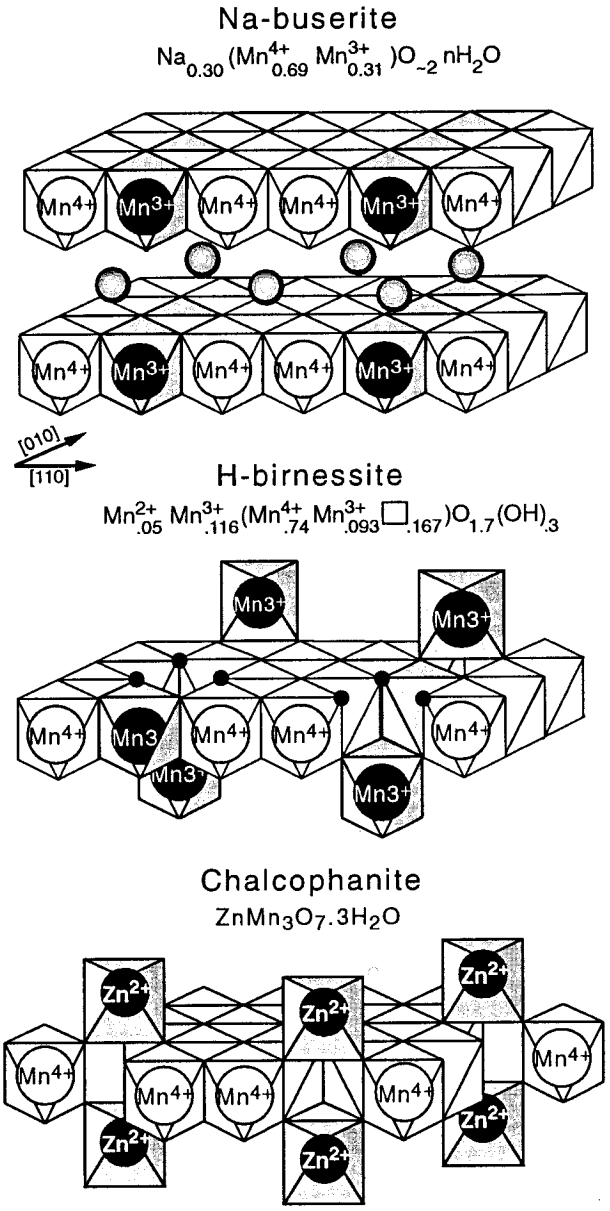

FIGURE 1. Idealized structures of monoclinic Na-exchanged buserite, hexagonal H-rich birnessite, and chalcophanite, after Drits et al. (1997), Silvester et al. (1997), Wadsley (1955), and Post and Appleman (1988). Chemical compositions given for NaBu and HBi correspond to averaged values for microcrystallites type I and II.

STRUCTURAL CHEMISTRY OF BUSERITE AND BIRNESSITE

The structural study of buserite and birnessite minerals has been a topic of sustained interest for the last ten years (Chukhrov et al. 1989; Chukhrov et al. 1985; Drits et al. 1997; Kuma et al. 1994; Manceau et al. 1992; Post and Veblen 1990; Silvester et al. 1997). In this section the main structural and chemical features of these phyllomanganates, as determined by Drits et al. (1997) and Silvester et al. (1997), are summarized.

Buserite and birnessite possess a layer structure formed of edge-sharing Mn octahedra (Fig. 1). Na-exchanged buserite, hereafter referred to as NaBu, contains two H_2O layers giving a characteristic 10 Å periodicity along the *c* axis. Its layer has an orthogonal unit cell with $a = 5.23$ and $b = 2.85$ Å, and is free of vacancies (Fig. 1). The average composition of NaBu is $Na_{0.30}(Mn^{IV}_{0.69}Mn^{III}_{0.31})O_{\sim 2}$. Partial dehydration of 10 Å NaBu leads to the formation of the one-layer monoclinic structure of Na-exchanged birnessite (hereafter referred to as NaBi), with sub-cell parameters $a = 5.173$, $b = 2.850$, $c = 7.342$ Å, and $\beta = 103.2°$. The average chemical composition of NaBi is $Na_{0.30}Mn^{2+}_{0.05}(Mn^{4+}_{0.74}Mn^{3+}_{0.21}\square_{0.05})O_{\sim 2}$, where $\square$ denotes vacant structural sites. NaBi consists in fact of two types of microcrystals, each having different structural formulae and layer cell parameters. NaBi type I is characterized by the structural formula $Na_x(Mn^{4+}_{1-x}Mn^{3+}_x)O_{\sim 2}$ with $0.16 \leq x \leq 0.25$, and the parameters $A = 3a = 15.52$ Å, $b = 2.85$ Å, and $\gamma = 90°$. NaBi type II has a better constrained structural formula $Na_{0.333}Mn^{2+}_{0.055}(Mn^{4+}_{0.722}Mn^{3+}_{0.222}\square_{0.055})O_{\sim 2}$ with $A = 3a = 15.52$ Å, $B = 3b = 8.55$ Å, and $\gamma = 90°$. The supercell $A = 3a$ arises from the ordered distribution of Mn^{3+}-rich rows parallel to [010] and separated from each other along [100] by two Mn^{4+} rows. Mn^{3+}-rich rows of NaBi type I and type II contain some Mn^{4+} distributed regularly with a periodicity of 6*b*. As microcrystals of type II are the dominant form in the NaBi samples, the average chemical composition of the powder is very close to the structural formula for NaBi type II. However it should be kept in mind that the structural formula for NaBi type I is inaccurate, and therefore the relative proportions of each NaBi type cannot be determined precisely. As a consequence, in the rest of the paper the results are discussed using either the average composition of NaBi or the structural formula of NaBi type II. It is assumed that the structural formula for NaBu that serves as a matrix for the formation of NaBi type II is $Na_{0.33}(Mn^{4+}_{0.67}Mn^{3+}_{0.33})O_2$. Again, this formula is very close to the average composition of NaBu.

H-rich birnessite (HBi), the low-pH form of birnessite, is obtained by equilibrating an NaBu suspension under acidic conditions. Species synthesized at pH = 4 have the unit-cell parameters $a = 2.848$, $c = 7.19$ Å, $\gamma = 120°$ and composition $Mn^{2+}_{0.05}Mn^{3+}_{0.116}(Mn^{4+}_{0.74}Mn^{3+}_{0.093}\square_{0.167})O_{1.70}(OH)_{0.30}$. In contrast to NaBu and NaBi, layers of HBi have an hexagonal symmetry and contain a considerable amount of octahedral vacancies. Interlayer cations are located either above or below vacant sites.

The transformation of NaBu to HBi in aqueous solution is more complex and is not completely understood (Fig. 2). It is characterized by an initial rapid process in which part of the interlayer Na is exchanged with H^+ from solution and 0.1 layer Mn^{3+} per octahedron disproportionate to Mn^{4+} and Mn^{2+} according to: $Mn^{3+} + Mn^{3+} \rightarrow Mn^{4+} + Mn^{2+}$ (Fig. 2), with Mn^{2+} migrating into so-

lution. Following this initial transformation, the structural formula of crystallites of type II can be written: $Na^{+}_{0.333-x}(Mn^{4+}_{0.722}Mn^{3+}_{0.223}\square_{0.055})O_{2.0-0.11-x}(OH)_{0.11+x}$ (Fig. 2b). A slower exchange process then ensues, in which the remainder of the interlayer Na desorbs and, depending upon the solution pH, Mn^{2+} re-adsorbs above or below vacancies: At pH = 5 all desorbed Mn^{2+} is re-adsorbed, whereas at pH = 2 no re-adsorption occurs. Associated with this slower exchange process is the migration of about one-half of the remaining layer Mn^{3+} atoms to the interlayer space located above or below newly formed vacancies. At equilibrium, the disproportionation and migration reactions result in a 50% occupancy of layer cation positions along the initial Mn^{3+}-rich rows. Because these rows alternate with two successive Mn^{4+} rows, the proportion of vacant sites in the structure is $\frac{1}{6}$ = 0.167 and the structural formula of HBi type II at pH 5 is $Mn^{2+}_{0.055}$-$Mn^{3+}_{0.112}(Mn^{4+}_{0.722}Mn^{3+}_{0.111}\square_{0.167})O_{1.67}(OH)_{0.33}$ (Fig. 2c).

Materials and methods

Sample preparation

NaBu was prepared following the procedure of Giovanoli et al. (1970). The solid phase was washed by centrifugation (more than six times) until the supernatant pH was approximately 9–10. Co sorption was achieved by adding a $Co(NO_3)_2$ solution to an NaBu suspension at pH 4. All samples were prepared in an argon-gas-saturated and constant ionic strength (0.1 mol/dm^3 $NaNO_3$) aqueous medium at 25 °C. The NaBu was not pre-equilibrated at pH 4 and, consequently, the low pH transformation of NaBu to HBi (Silvester et al. 1997) and the sorption of Co occurred simultaneously. The Co concentration in solution was adjusted to obtain different Co/Mn molar ratios of 0.06 (S1), 0.14 (S2), and 0.24 (S3) on solids. After allowing several hours for equilibration, S1 and S3 samples were filtered, rinsed, and dried, yielding Co-containing birnessite (CoBi) solids. S2 was prepared as a self-supported oriented film (Silvester et al. 1997). Total Co concentrations were determined by inductively coupled plasma (ICP) spectroscopy after dissolution of the dried solids in hydroxylamine hydrochloride ($NH_3OH{\cdot}Cl$).

X-ray diffraction

Powder X-ray diffraction patterns were recorded on a Siemens D5000 diffractometer equipped with a Si(Li) solid-state detector. Cu$K\alpha$ radiation was used with a counting time of 20 or 30 s per 0.04° 2θ step. The absolute precision of Bragg angles was determined with a quartz standard and was found to be better than 0.01° 2θ over the full angular range.

Because of the high density of defects the Rietveld approach cannot be applied, and one of the most effective ways of revealing the fine structural and chemical features of disordered layer minerals is by simulating diffraction patterns from realistic structural models (Drits and Tchoubar 1990). The program used for simulating XRD patterns was written by A. Plançon at the University of Orléans. It is based on the mathematical formalism

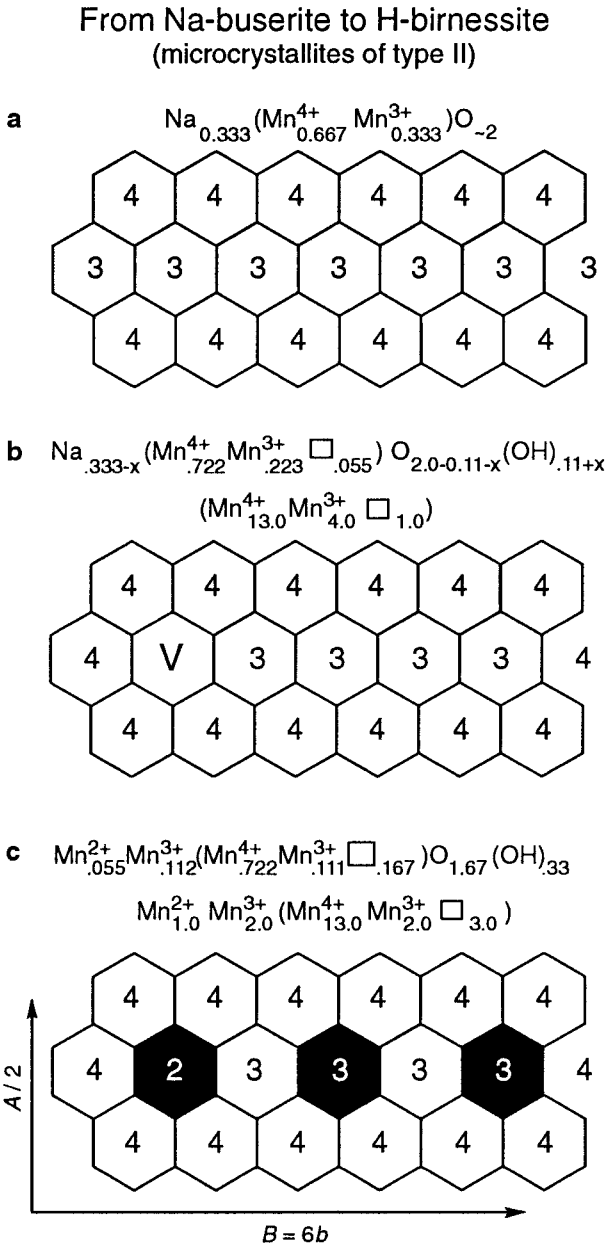

Figure 2. Schematic structural representation of the low pH transformation from monoclinic NaBu type II to hexagonal HBi type II. Half super-cell projected in the *a*-*b* plane. Interlayer octahedra are drawn in black. The oxidation state of Mn is indicated by arabic numbers.

described by Plançon (1981), Sakharov et al. (1982a, 1982b), and Drits and Tchoubar (1990). Calculations were performed for the 10*l* reflections, which are the most sensitive to site occupancy. Coherent-scattering domains (CSD) in the layer plane have a disk-like shape, the mean radius of which was determined by fitting the 100 reflection. The CSD size distribution along the *c* axis was quantified by two parameters, the average (N_{Mean}) and maximum (N_{Max}) number of layers (Reynolds 1989). Where

necessary, random stacking faults were introduced and their amount adjusted with the W_R probability parameter.

According to the structural model (space group $P\bar{3}$) described by Chukhrov et al. (1985) the unit cell of the one-layer birnessite contains one cation and two O sites within the layer and two cations and two H_2O sites within the interlayer. The *x* and *y* coordinates of these sites were fixed to values corresponding to the hexagonal symmetry. Starting values for *z* coordinates were set to those of Chukhrov et al. (1985) and were further refined during the fitting process.

Powder and polarized EXAFS

Co and Mn *K*-edge EXAFS spectra were recorded at the LURE synchrotron radiation laboratory (Orsay, France) on the EXAFS 1 station. The positron energy of the DCI storage ring was 1.85 GeV and the current between 280 and 320 mA. The incident X-ray beam was monochromatized with a channel cut Si(331) crystal. X-ray absorption data for Mn and Co were recorded over the energy ranges 6400–7400 eV and 7600–8400 eV, respectively. Over these energy ranges the Bragg angle varied from 51° to 36°. Within this angular range the polarization rate of X-rays is almost 100% (Hazemann et al. 1992). Measurements were performed in transmission mode with the beam intensity measured by gas ionization. Ionization chambers were filled with an air-helium mixture, proportioned to attenuate the beam intensity by ~20% before and ~50% after the samples. Special care was taken to avoid sample thickness and heterogeneity effects in the collection of EXAFS spectra (Manceau and Gates 1997; Stern and Kim 1981). Polarized EXAFS spectra were recorded on a flat self-supported CoBi film. Angular measurements were made by turning film layers around a rotation axis normal to both the beam direction and the electric field vector $\boldsymbol{\epsilon}$. The angle (α) between $\boldsymbol{\epsilon}$ and the layer plane was varied from 0° to 60°. The function $\chi(\alpha = 90°)$ was calculated by linear regression using the formula $\chi(\alpha) = [\chi(0°) - \chi(90°)]\cos^2\alpha + \chi(90°)$ (Brouder 1990; Heald and Stern 1977; Manceau et al. 1988). Powder EXAFS spectra were recorded at $\alpha = 35°$ to eliminate any texture effects originating from possible preferential orientation of birnessite platelets (Manceau et al. 1990).

X-ray absorption spectra were normalized and the EXAFS spectra then Fourier-filtered according to standard procedures (Teo 1986). A Kaiser-function window was used in Fourier transforms to minimize the intensity of side lobes resulting from truncation effects (Manceau and Combes 1988). Co-O, Mn-O, and Mn-Mn distances and the number of atoms in nearest O (CN_O) and Mn (CN_{Mn}) coordination shells were determined by using experimental phase shift and amplitude functions derived from CoOOH and a stoichiometric λ-MnO_2 reference. In CoOOH, Co^{3+} is surrounded by six O atoms at 1.90 Å and six nearest Co atoms at 2.85 Å (Delaplane et al. 1969). In λ-MnO_2, Mn^{4+} is surrounded by six nearest O atoms at 1.91 Å and six nearest Mn atoms at 2.84 Å (Thackeray et al. 1993). In the absence of a suitable reference for Co-Mn pairs, McKale's phase shift functions were used for calculating Co-Mn distances. The accuracy of these functions was tested by comparing EXAFS derived atomic distances with the crystallographic values for Co-Co and Mn-Mn distances in CoOOH and λ-MnO2. For these two compounds the EXAFS distances differed by less than 0.01 Å from the crystallographic values. The absolute accuracies of interatomic distances and number of atomic neighbors determined in this study are estimated to ±0.02 Å and ±10% for the oxygen shell, ±0.02 Å and 20% for the nearest cation shell, and ±0.04 Å and 30% for the next-nearest cation shell. The relative accuracy between samples is better.

The amplitude of polarized EXAFS spectra, and accordingly of RSF peaks, depends on the angle that the particular atomic pair makes with the electric field vector $\boldsymbol{\epsilon}$. This angular dependence can be written:

$$\chi(k, \theta) = \sum_j \sum_{i=1}^{N_j} 3\cos^2(\theta_i^j)\chi_{iso}^j(k) \quad (1)$$

where *j* is the number of the neighboring atomic shell, *i* runs over all the CN_j atoms of the *j*th shell, θ_j^i is the angle between the polarization vector $\boldsymbol{\epsilon}$ and the vector r_j^i that binds the absorbing atom to the *i*th atom of the *j*th shell, and χ_{iso} is the isotropic (i.e., powder) contribution of the *j*th shell. For a completely random powder, there is no angular variation, and $\chi(k,\theta)$ is reduced to:

$$\chi(k) = \chi(k, \theta) = \sum_j \chi_{iso}^j(k).$$

It is a direct result from Equation 1 that P-EXAFS experiments can provide unique angular structural information and can be used to probe the in-plane and out-of-plane structure of phyllomanganates. The quantitative interpretation of P-EXAFS spectra is examined in the case of an idealized phyllomanganate layer. In the layer plane Mn-Mn_1 pairs across edges are rotated by 60°, so for the in-plane orientation of the electric vector $\boldsymbol{\epsilon}$ ($\alpha = 0°$),

$$CN_{Mn\text{-}Mn_1}^{\alpha=0°} = \sum_{i=1}^{6} 3\cos^2(\theta_i) = 9$$

instead of six for a powder spectrum (Fig. 3a). Regardless of the orientation of $\boldsymbol{\epsilon}$ within the layer plane, the apparent number (CN_{app}) of nearest Mn atoms is 1.5 times greater than the crystallographic number (CN_{cryst}). It can be easily demonstrated that this factor also holds whenever $CN_{cryst} < 6$, that is in the presence of layer vacancies, provided that there is a threefold, or higher, symmetry axis perpendicular to the layer plane. For the out-of-plane orientation ($\boldsymbol{\epsilon} \parallel c^*$, $\alpha = 90°$), the contribution of Mn-Mn_1 pairs is zero because $\theta = 90°$. Mn-Mn_2 pairs across corners have a different angular dependence (Fig. 3b). The six vectors connecting an Mn atom located above or below a vacancy to the six layer Mn_2 make an identical β angle with the c* direction. Thus, for the out-of-plane orientation of the electric vector,

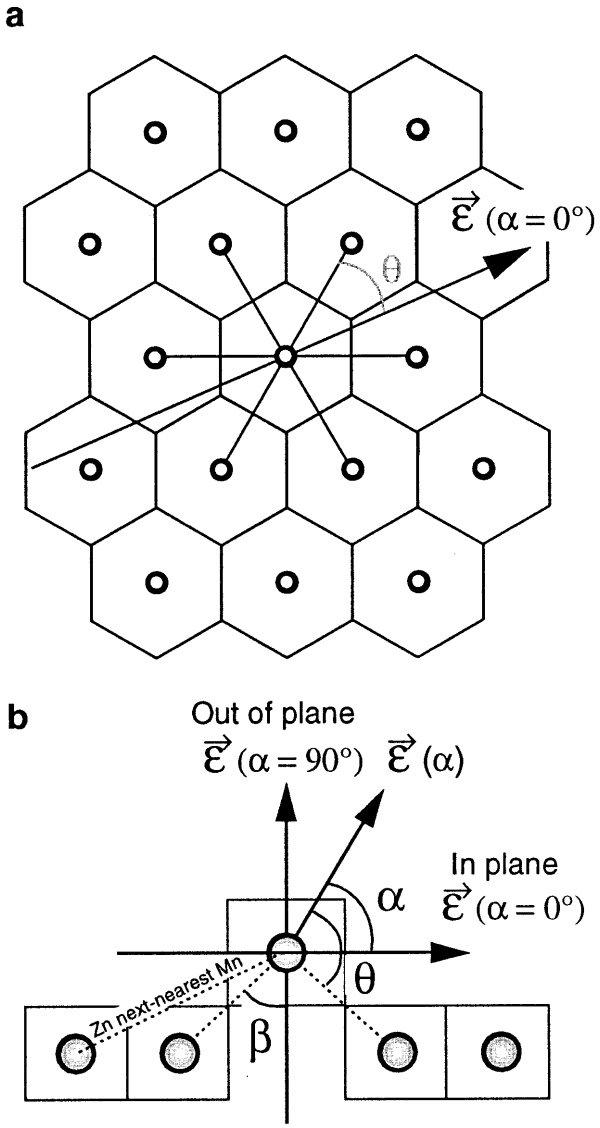

FIGURE 3. Possible relative orientations of a phyllomanganate layer to the electric field vector **ϵ**. (**a**) projection in the *a*-*b* plane; (**b**) projection in the *b*-*c* plane. α is the angle between the layer and **ϵ**, β is the angle between the vector connecting the atomic pair of interest and the perpendicular to the layer, and θ is the angle between the vector connecting the atomic pair of interest and **ϵ**.

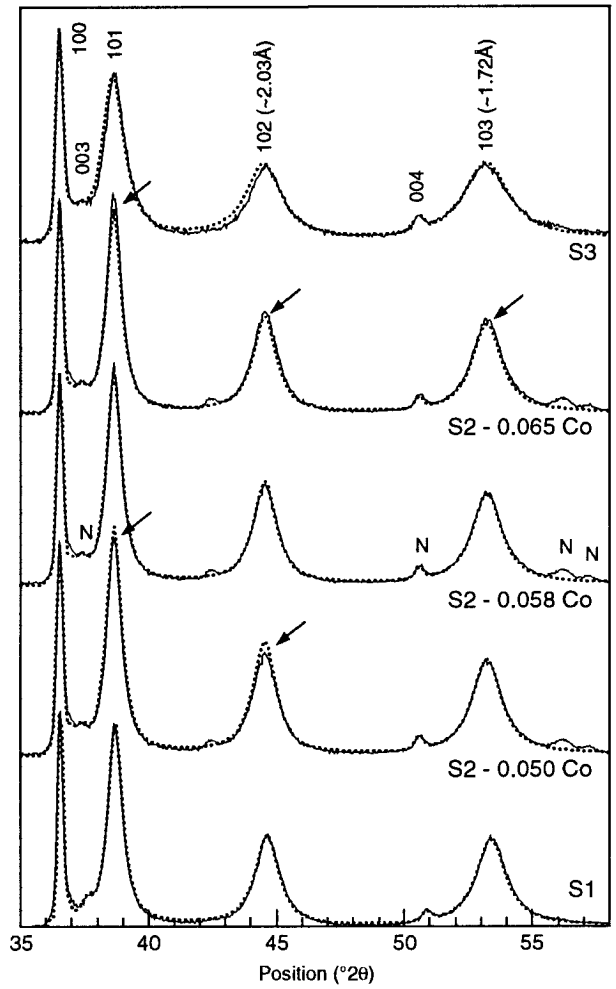

FIGURE 4. Agreement between experimental (dots) and calculated (solid line) XRD profiles. The comparison is for 10*l* reflections ($l \leq 3$). Simulation parameters are listed in Table 3. The influence of the interlayer cation site occupancy on the distribution of intensity for calculated XRD profiles is illustrated for sample S2. Site occupancy was varied from 0.050 to 0.065, whereas the optimum value is 0.058. Arrows indicate discrepancies between experimental and calculated intensity distributions. Intensities are normalized to 100 for the 100 reflection. Cu$K\alpha$ X-ray radiation.

$$CN^{\alpha=90^\circ}_{\text{Mn-Mn}_2} = \sum_{i=1}^{6} 3\cos^2(\theta_i) = 18\cos^2\beta.$$

It is a particularly important result that if $\beta = 54.7°$, $CN_{\text{Mn-Mn}_2} = 6$, as in the powder. The calculation of $CN^{\alpha=0^\circ}_{\text{Mn-Mn}_2}$ is less straightforward since each of the six atomic pair vectors makes a different θ angle for a given orientation of **ϵ** in the layer plane. Manceau et al. (1990) showed that when the atomic pair under consideration (e.g., Mn-Mn_2) possesses at least a threefold axis perpendicular to the layer plane, $\chi(k,\theta)$ is independent of the position of **ϵ** within the layer plane. In this case, by averaging over the in-plane angles, it is possible to eliminate θ, yielding the following formula:

$$\langle\cos^2\theta_i\rangle = \cos^2\beta\,\sin^2\alpha + (\sin^2\beta\,\cos^2\alpha)/2 \qquad (2)$$

The relationship between CN_{cryst} and CN_{app} can then be written (Manceau et al. 1990):

$$CN_{\text{app}} = 3\,CN_{\text{cryst}}\,[\cos^2\beta\,\sin^2\alpha + (\sin^2\beta\,\cos^2\alpha)/2] \qquad (3)$$

These equations are valid provided that the atomic pair under study makes at least a threefold axis with the layer plane. In self-supporting films, the rotation of platelets in the *a*-*b* plane results in an ∞ axis parallel to c* and, con-

TABLE 1. Unit-cell parameters determined for various Co-sorbed birnessite samples

	S1	S2	S3	HBi
$[Co]_{solution}$	10^{-3}	5×10^{-3}	2×10^{-2}	—
$(Co/Mn)_{solid}$	0.06	0.14	0.24	—
a (Å)	2.838	2.840	2.842	2.848
c (Å)	7.180	7.212	7.215	7.189

Note: H-rich birnessite data are from Drits et al. (1997).

sequently, this condition is fulfilled. It can be easily verified that Equations 1 and 2 give the same result, but Equation 2 is much easier to apply as it directly connects experimental α values to crystallographic β angles. Accordingly, from the knowledge of β it is possible to calculate CN_{app} for every α angle. A particularly important result is that for $\alpha = 35.3°$, $\langle \cos^2\theta_i \rangle = \frac{1}{3}$ and

$$\chi(k) = \chi(k, \theta) = \sum_j \chi^j_{iso}(k),$$

regardless of the β angle. Thus the powder EXAFS spectrum of a solid may be readily recorded from a self-supported film oriented at $\alpha = 35.3°$. Similarly, if an atomic pair makes a β angle of 54.7°, then this is geometrically equivalent to an α angle of 35.3°, in which case $CN_{app} = CN_{cryst}$. The value $\beta = 54.7°$ is a magic angle for which the EXAFS amplitude of the considered pair is independent of the orientation of the sample in the X-ray beam. For $\beta < 54.7°$, $\chi(k,\alpha)$ increases with α, whereas for $\beta > 54.7°$, $\chi(k,\alpha)$ decreases with increasing α. This contrasting variation of $\chi(k,\alpha)$ with β was recently demonstrated experimentally for the smectite nontronite (Manceau et al., in preparation).

RESULTS

XRD

Qualitative analysis. Powder XRD patterns for CoBi samples are shown in Figure 4. These patterns are quite similar to those reported by Chukhrov et al. (1985) and Drits et al. (1997) for natural and synthetic one-layer hexagonal birnessite. Note that S2 contains some nsutite (γ-MnO_2) impurity. The unit-cell parameters increase systematically with increasing Co content (Table 1). Experimental and calculated d_{hkl} values are given in Table 2. The XRD patterns contain diagnostic 102 and 103 peaks (2.03 and 1.72 Å, respectively; Fig. 4). The similar intensities of these peaks indicate the presence of large amounts of interlayer cations lying above or below vacant sites (Chukhrov et al. 1985). The relative intensity and profile shape of the *hkl* reflections vary with Co loading. In particular, 10*l* reflections of sample S3 are broader and weaker than S1 and S2 indicating a decrease in the three-dimensional (3D) ordering due to the presence of stacking faults.

Comparison of experimental and calculated patterns. Experimental and calculated patterns are shown in Figure 4. The corresponding structural parameters are listed in Table 3. All experimental XRD patterns (10*l* reflections, $l \leq 3$) are correctly reproduced by the simulation. The extreme sensitivity of calculated XRD profiles to site occupancy is illustrated in Figure 4. This figure illustrates the dramatic effect of a small variation of the interlayer cation occupancy (from an optimum value of 0.058, to 0.050 and 0.065, respectively) on the intensity distribution. With these results, the estimated error in cation site occupancy is less than 0.01. The fitted structural parameters reported in Table 3 confirm that a high proportion of vacancies is overlaid by interlayer cations. Variations in the amount of interlayer cations, vacancies, and stacking faults as a function of Co content may be described as follows.

TABLE 2. X-ray powder data for Co-sorbed birnessite

	S1		S2		S3	
hkl	d_{hkl}(calc)	d_{hkl}(exp)	d_{hkl}(calc)	d_{hkl}(exp)	d_{hkl}(calc)	d_{hkl}(exp)
001	7.180	7.193	7.212	7.222	7.215	7.212
Nsutite				3.961		
002	3.590	3.585	3.606	3.606	3.608	3.607
100	2.458	2.459	2.460	2.460	2.461	2.460
003/Nsutite	2.393	2.388 w	2.404	2.405 w		2.386 w
101	2.325	2.328	2.328	2.330	2.329	2.330
Nsutite				2.131		
102	2.028	2.031	2.032	2.033	2.033	2.032
004	1.795	1.795	1.803	1.804	1.804	1.805
103	1.715	1.717	1.719	1.722	1.720	1.723
Nsutite				1.638		
Nsutite				1.613		
104	1.450	1.451	1.454	1.454	1.455	1.459 vb
110	1.419	1.419	1.420	1.420	1.421	1.421
111	1.392	1.394	1.393	1.395	1.394	1.398
112	1.320	1.320	1.321	1.325	1.322	1.326
105	1.240	1.240 vb	1.244	1.246 b	1.245	vb
200	1.229	1.229	1.230	1.230	1.231	1.230

Notes: Spacings in Å. Theoretical values are calculated for the various sets of unit-cell parameters given in Table 1.

(1) The cation site occupancy within layers increases strongly from 0.83 (Co-free HBi) to 0.89 (S1) and 0.90 (S2 and S3). Associated with this increase in layer occupancy is an initial decrease in the amount of interlayer cations from 0.167 (Co-free HBi) to 0.11 (S1). At higher Co levels the amount of interlayer cations again increases to 0.13 (S3). For the lower Co content (S1) the amount of interlayer cations exactly matches the amount of vacancies. For higher Co contents, the amount of interlayer cations is higher than the amount of vacancies, and it is necessary to locate interlayer cations above and below some layer vacancies.

(2) With increasing Co, the *a* parameter first decreases from 2.848 Å (Co-free HBi) to 2.838 Å (S1). The *a* parameter then increases with increasing Co content. This behavior may be related to the evolution of the interlayer occupancy that, as noted above, strongly decreases at first and then increases again. Another important parameter that may be related to the increase of the *a* parameter with increasing Co content is the ratio of interlayer cations located above and below vacancies relative to interlayer cations located above or below vacancies. This ratio increases from 0 (S1) to 0.50 (S2) and to 0.86 (S3).

(3) The average cation-oxygen distances within layers

TABLE 3. Structural parameters used for the simulation of X-ray diffraction profiles

		S1	S2	S3
	Mean *N*	8	8	9
	Max *N*	30	30	30
	Radius	220	170	155
	W_R	0.23	0.22	0.40
O (position d)	*x*	0.667	0.667	0.667
	y	0.333	0.333	0.333
	z	1.02	1.02	1.02
	Occupancy	1.00	1.00	1.00
Mn or Co within layer (position a)	*x*	0	0	0
	y	0	0	0
	z	0	0	0
	Occupancy	0.89	0.90	0.90
Mn or Co interlayer (position c)	*x*	0	0	0
	y	0	0	0
	z	2.05	2.05	2.05
	Occupancy	0.06	0.058	0.065
H_2O (position d)	*x*	−0.667	−0.667	−0.667
	y	−0.333	−0.333	−0.333
	z	3.47	3.47	3.47
	Occupancy	0.30	0.25	0.27
Bond length (Å)	Mn-O	1.93	1.93	1.93
	O-Mn_{int}	1.94	1.94	1.94
	Mn_{int}-H_2O	2.17	2.17	2.17
	H_2O-$O_{next\ layer}$	2.69	2.72	2.73
	$(Mn,Co)_{layer}$-$(Mn,Co)_{interlayer}$	3.50	3.50	3.50

Notes: All parameters were adjusted to fit the experimental profiles (Fig. 4). The *x* and *y* coordinates are expressed in fraction of *a* and *b* parameters, respectively; *z* and bond lengths are expressed in Å, to emphasize the thickness of layer and interlayer octahedra. The radius of the CSDs in the *a-b* plane are also expressed in Å, whereas CSDs along *c** (*N*) are given in layers. W_R is the proportion of random stacking faults. Positions and occupancies are given for the $P\bar{3}$ space group.

are about the same for all samples (~1.93 Å). The average distances from interlayer cation to O atom (1.94 Å), on the one hand, and to H_2O molecule (2.17 Å), on the other hand, are quite similar for all samples, as the average thickness of interlayer octahedra is constant. The average distance between layer and interlayer cations is 3.50 Å (Table 3). This value is indicative of a tridentate corner linkage, as in chalcophanite where *d*(Zn-Mn) = 3.55 Å (Fig. 1) (Wadsley 1955).

(4) The amount of stacking faults generally increases from S1 (W_R = 0.23) and S2 (W_R = 0.22) to S3 (W_R = 0.40). No regular trend could be observed between the Co concentration and the amount of stacking faults.

Powder EXAFS

Qualitative analysis. EXAFS spectra and radial structure functions (RSFs) for the different CoBi samples are shown in Figures 5 and 6 and compared to those of Co-containing asbolane and lithiophorite (Manceau et al. 1987). Mn and Co *K*-edge EXAFS and RSFs for S1 are very similar to those observed for natural samples. Specifically, the characteristic shape of the Co *K*-edge signal in the range 4–5.5 $Å^{-1}$ (arrows) observed for asbolane and lithiophorite (Fig. 3 in Manceau et al. 1987) is reproduced at low Co sorption. This salient result indicates that the peculiar crystal chemical behavior of Co atoms found in natural manganese oxides was reproduced in the laboratory. The amplitude of the Co *K*-EXAFS signal and RSF peaks for S1 are markedly enhanced compared to Mn *K*-edge results. With increasing Co concentration, two spectral modifications are noticed. First, the relative amplitudes of Co and Mn waves are reversed (Fig. 5). This evolution can be clearly observed in the respective RSFs where the intensities of the first two Co peaks drop while those for the Mn peaks increase (Figs. 6, 7). Second, the shoulder at 6.3 $Å^{-1}$ becomes progressively more intense and appears as a resolved oscillation maximum on the S3 spectrum (arrows, Fig. 5). It will be shown later that this spectral evolution accounts for the increase of 3rd peak in the Co RSFs at increasing Co loading. The Mn RSFs for the low Co sample (S1) and HBi compare closely with one another. At higher Co contents the amplitude of the second peak in the Mn RSFs increases. This trend is really noteworthy as it indicates that the sorption of Co modifies the Mn-Mn contributions across edges. Stated another way, the results show that Co readily interacts with birnessite layers, being either surface adsorbed or trapped within Mn^{4+} layers, and does not precipitate as cobalt (oxyhydr)oxide.

Quantitative analysis: Nearest O shell. RSF peaks were singled out and Fourier back-transformed from distance space (*R*) to the wavevector space (*k*). This mathematical operation yields a partial EXAFS spectrum, that is, the contribution to the whole EXAFS spectrum of the selected atomic shells. Co-(O,OH,OH_2) and Mn-(O,OH,OH_2) (hereafter noted Co-O and Mn-O) contributions to EXAFS spectra were filtered by selecting the first peaks in the Co and Mn RSFs, respectively.

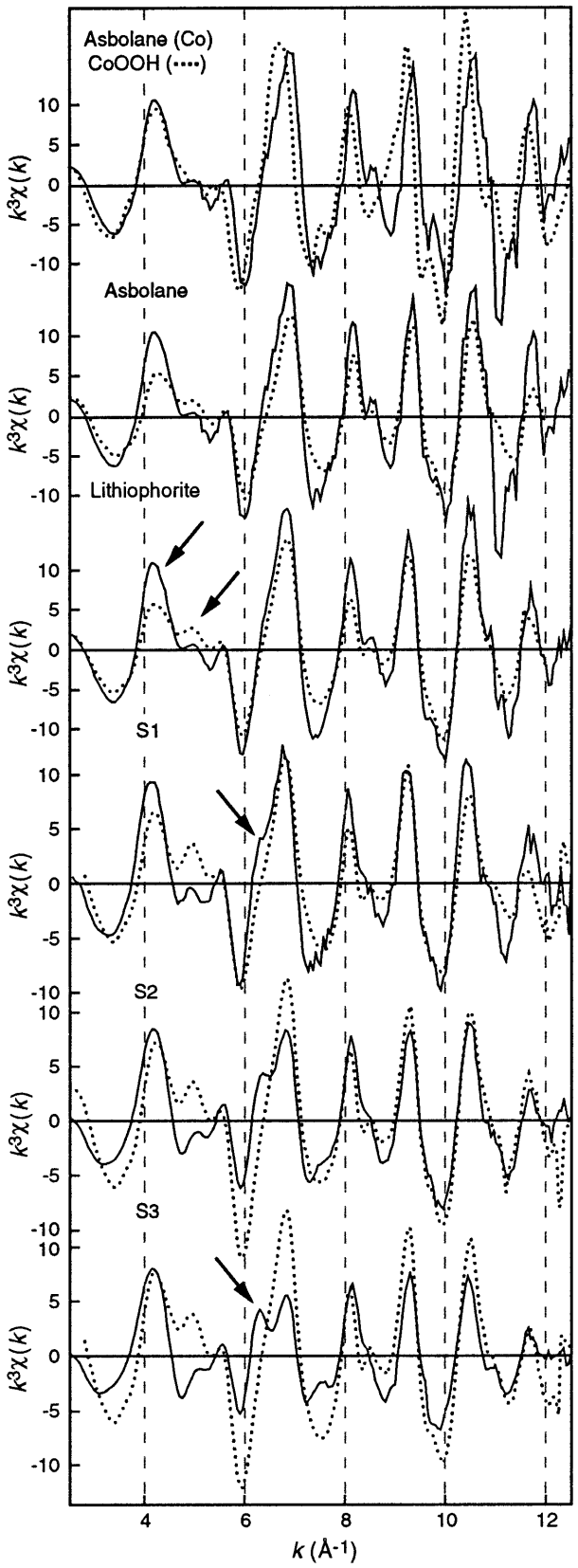

FIGURE 5. Various k^3-weighted Co and Mn *K*-edge EXAFS spectra for CoOOH, asbolane, lithiophorite, and Co-sorbed birnessite. Solid line = Co *K* edge; dotted line = Mn *K* edge except in the case of CoOOH (Co *K* edge). Asbolane and lithiophorite spectra are from Manceau et al. (1987).
←

Figure 8a shows that Co-O pairs for the Co-sorbed samples do not have the same wave amplitude and frequency as the reference CoOOH. Increasing the Co loading results in a beat node pattern at 9–10 $Å^{-1}$, which indicates the presence of multiple wave frequencies and, therefore, of several O shells around Co. Consequently, the spectral fitting of S2 and S3 requires a minimum of two shells. The spectra were sucessfully fitted (Q = 0.01–0.015, Table 4) by assuming a short Co-O distance of 1.91 Å typical of low-spin Co^{3+}-O bonds, and a larger of 2.09 Å typical of the high spin Co^{2+}-O pair. The percentage of Co^{3+} in S2 and S3 was evaluated from the number of O atoms in each sub-shell and was found to be 80 ± 10% and 70 ± 10%, respectively. As demonstrated by the strong wave beating of Figure 8a, in this particular system the sensitivity of EXAFS to the Co^{3+}/Co_{tot} ratio is high as a result of the strong phase contrast between Co^{3+}-O and Co^{2+}-O pairs, which are separated by 0.18 Å. In contrast to S2 and S3, S1 does not display a marked beat pattern, and its electronic wave is almost in phase with CoOOH. S1 essentially differs from CoOOH by a lower wave amplitude, which indicates that Co-O distances show a greater spread in S1 than in the reference. These observations led us to suspect the presence of some Co^{2+}-O pairs in this sample, but in an amount that is too low to give rise to wave beating. Consequently, S1 was fitted by assuming a single O shell. The spectral simulation yielded 5.5 O at 1.92 Å and a Debye-Waller factor (σ) logically slightly greater than for the other samples ($\Delta\sigma$ = 0.03 Å vs. 0.00–0.01 Å). In this sample, the maximum amount of Co^{2+} was estimated by independently varying *CN* and σ during the fit, and was evaluated to be 10%. In conclusion, the spectral analysis of the first O shell provides compelling evidence for the oxidation of divalent Co at the birnessite surface. Examination of Table 4 shows that the percentage of Co^{3+} decreases with increasing Co loading, which points to a decreasing capacity of birnessite to oxidize Co with increasing surface coverage.

Hexagonal and monoclinic birnessite possess substantial amounts of lower valency Mn (Mn^{2+} and Mn^{3+}) cations (Drits et al. 1997; Silvester et al. 1997). The multiplicity of Mn structural environments is a source of disorder that tends to lower the amplitude of the wave backscattered by nearest O atoms as previously observed at the Co *K* edge for S1. This disorder effect results in both an increase in the Debye-Waller factor (σ) and an apparent reduction of coordination numbers (*CN*), arising from the high correlation between *CN* and σ (Teo 1986). These considerations are illustrated in Table 4, which

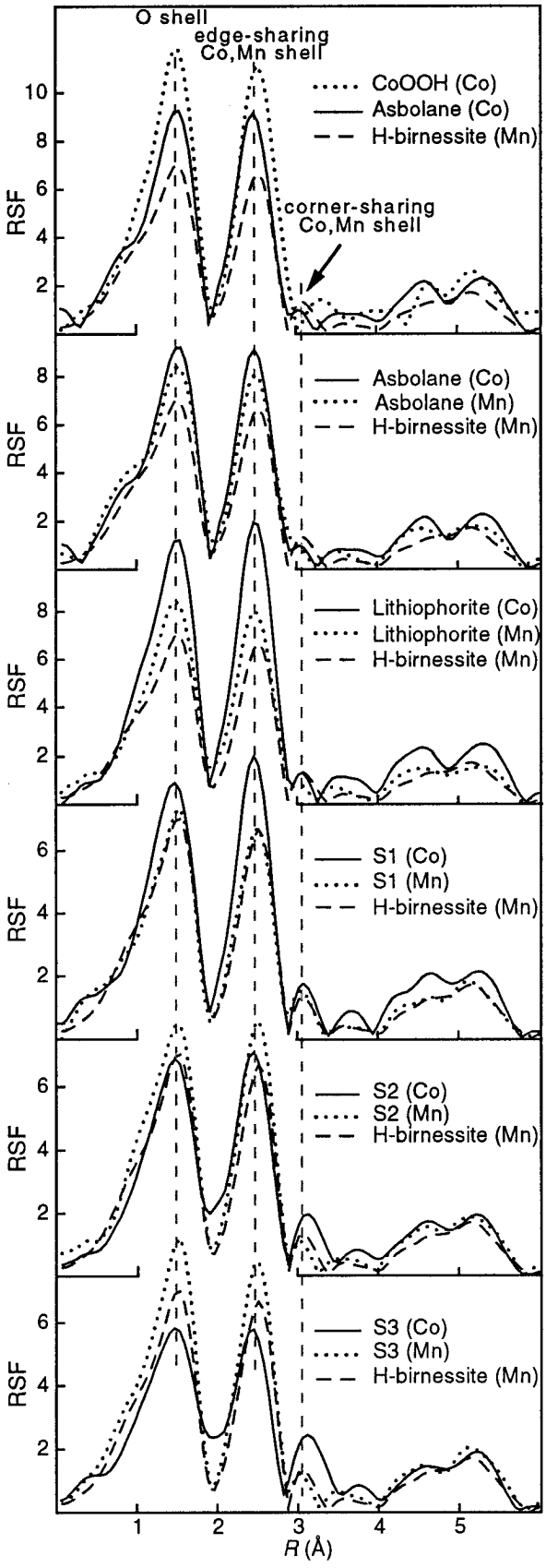

FIGURE 6. Radial structure functions (RSF) from EXAFS measurements for asbolane, lithiophorite, H-rich birnessite, and Co-sorbed birnessite. Solid line = Co *K* edge; dotted and dashed line = Mn *K* edge except in the case of CoOOH (Co *K* edge). The *K* edge is indicated in parenthesis. First peaks correspond to the O shell, second peaks to the Co,Mn edge-sharing contribution, and the weak third peak near 3 Å to the Co,Mn corner-sharing contribution. RSFs were not corrected for phase shift; accordingly peaks are shifted toward shorter distances by $\Delta R \approx$ 0.3–0.4 Å with respect to crystallographic values. Real distances obtained from least-squares fits are reported in Tables 4 and 5. ←

shows that for the Co-free hexagonal birnessite sample, $CN_{Mn\text{-}O} = 4.7$, instead of the crystallographic value of six, and $\Delta\sigma = 0.01$ Å, instead of 0.0 in the non-disordered λ-MnO_2 reference. The increase of $CN_{Mn\text{-}O}$ from 4.2 (S1) to 5.3 (S3) with increasing Co concentration (Table 4) accounts for the enhancement of Mn-O RSF peaks noted in Figure 7a. This trend stands in strong contrast with that observed at the Co *K* edge since the average structural disorder about Co atoms because of their mixed valency (i.e., Co^{2+} plus Co^{3+}) increases with the Co concentration (Fig. 8b). In summary, the higher the Co content, the greater the valency mixture of Co atoms and the lower the valency mixture of Mn atoms. As discussed below, this interpretation is in good agreement with the evolution of structural formulae at increasing Co concentration.

The mean Mn-O distance of 1.91 Å is indicative of an overwhelming presence of tetravalent and trivalent Mn atoms. For example, in the tetravalent manganese oxides pyrolusite and ramsdellite, $\langle d(Mn^{4+}\text{-}O)\rangle = 1.89$ Å, whereas in the trivalent manganese oxide groutite (α-MnOOH) the four nearest $O_{equatorial}$ are located at ⟨1.93 Å⟩ and the two distant O_{apical} at 2.18 Å and 2.34 Å (Glasser and Ingram 1968). In the case of mixed-valency minerals, the contribution of the two distant Mn^{3+}-O_{apical} pairs is particularly weak and remains undetected. Mn^{2+}-O distances are typically 2.21 Å (Christensen 1965), but the number of divalent Mn atoms in birnessite samples is very low and only marginally influences mean Mn-O distances.

Quantitative analysis: Nearest (Co,Mn) shells. Fourier-filtered nearest Co-(Co,Mn) contributions for CoBi samples, obtained by selecting the second peak in the Co RSFs, are shown in Figure 8b. These curves, which correspond to edge-sharing octahedra, differ in their envelope amplitude but possess precisely the same phase, indicating that Co-(Co,Mn) distances are identical for the three samples. Because Co^{2+} and Co^{3+} octahedra have different sizes, the constancy in edge-sharing distance leads us to conclude that either Co^{2+} or Co^{3+} ions share edges with neighboring octahedra, but not both. Otherwise the simultaneous presence of Co^{2+}-(Co,Mn) and Co^{3+}-(Co,Mn) pairs would have shifted the wave frequency at increasing loading, similar to that observed for the Co-O contribution (Fig. 8a). Continuing this line of reasoning, given that Co in S1 is almost exclusively Co^{3+}

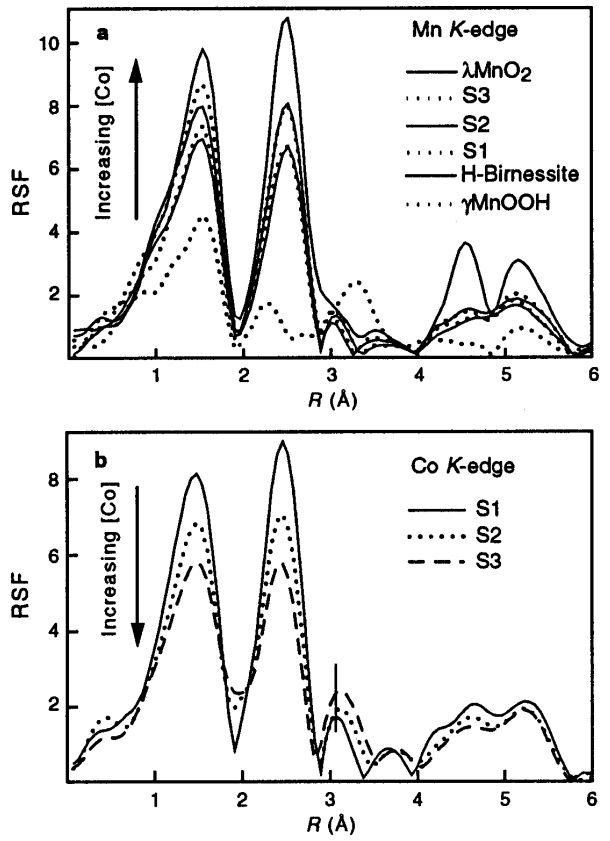

FIGURE 7. Comparison of Mn (**a**) and Co (**b**) *K*-edge RSFs for S1, S2, S3, and reference compounds. RSFs in (**a**) are labeled in decreasing amplitude at 1.5 Å.

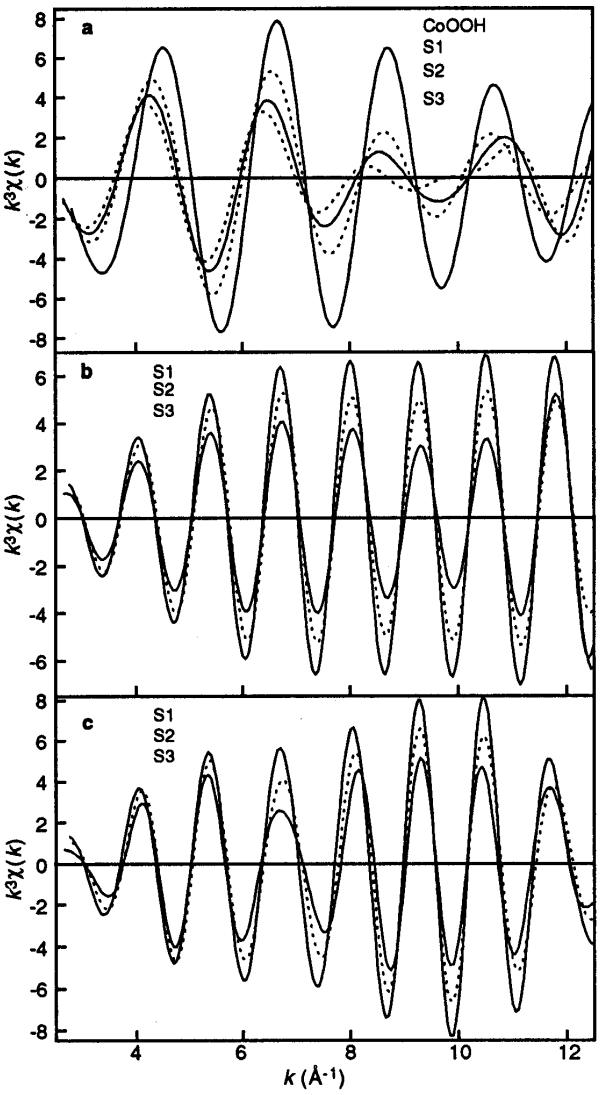

FIGURE 8. Fourier-filtered Co-O (**a**), Co-nearest (Mn,Co) (**b**), and Co-nearest plus next-nearest (Mn,Co) (**c**) contributions to EXAFS for Co-sorbed samples. Distance (*R*) window for (**a**) = 1.0 to 2.0; *R* window for (**b**) = 2.0 to 2.9, *R* window for (**c**) = 2.0 to 3.3–3.5. Names of samples are indicated in decreasing order of the wave amplitude at 4–8 Å^{-1}.

(Table 4), we may exclude the possibility of Co^{2+}-(Co,Mn) edge linkages. We are, therefore, left with two possibilities, either Co^{3+}-Co^{3+} or Co^{3+}-Mn^{4+} pairings across edges. The former hypothesis is ruled out for two reasons. First, the assumption of solely Co^{3+}-Co^{3+} pairs is equivalent to assuming the existence of Co-rich domains with a CoOOH structure, and, as we have seen, the S1 sample and CoOOH have a different Co local structure. Second, the sorption of Co atoms markedly modifies the local environment of Mn atoms (i.e., increase of $CN_{Mn\text{-}(Mn,Co)}$), and this structural perturbation can only be accounted for by assuming Co^{3+}-Mn pairings. Within the constraints of the phyllomanganate type structure, Co^{3+}-Mn edge-sharing pairings with $CN_{Co\text{-}(Mn,Co)} > 3$ could only be achieved by the migration of Co^{3+} into layer vacancies. As discussed below, these structural interpretations based on the analysis of nearest cation shells agree completely with results of the second cation shell analysis.

Mn-Me_1 (Me = Mn,Co) distances equal 2.86 Å, and Co-Me_1 distances 2.83–2.84 Å for all CoBi samples, the latter being consistent with the presence of trivalent Co in phyllomanganate layers (Table 5). EXAFS interatomic distances agree completely with *a* parameters determined by XRD (2.838–2.848 Å), taking into account an absolute precision of 0.02 Å for the second shell. Co-Me_1 distances are shorter than Mn-Me_1 by 0.02–0.03 Å, and this relative difference was found to be significant by superimposing Co and Mn *K*-edge experimental spectra for the different samples (data not shown). Comparison of the ionic radii of Mn^{4+} (0.53 Å) and Co^{3+}_{LS} (0.545 Å) does not provide a satisfactory explanation for this reduction of bond length. Discussed below, this difference in distance stems from a difference of Co^{3+} and Mn atomic environments.

It was noticed in Figure 7 that the intensity of the second peak in the Mn RSFs increased with increasing Co loading. This trend correlates well with an increase in Mn

TABLE 4. EXAFS parameters for Co-O and Mn-O pairs

Sample	*K* edge	*R* (Å)	CN_O	Δσ (Å)	Co^{3+}	*Q*
HBi	Mn	1.91	4.7	0.01		0.01
S1	Co	1.92	5.5	0.03	90–100%	0.01
	Mn	1.90	4.2	0.00		0.03
S2	Co	1.91	4.0	0.01	80 ± 10%	0.02
		2.09	1.0	0.00		
	Mn	1.91	5.1	0.00		0.02
S3	Co	1.91	4.1	0.01	70 ± 10%	0.02
		2.09	1.7	0.00		
	Mn	1.91	5.3	0.00		0.03

Notes: CN is the coordination number; Δσ is the difference of Debye-Waller factor between the sample and the reference. *Q* is the figure of merit for the spectral fitting: $Q = \Sigma(k^3\chi_{exp} - k^3\chi_{th})^2/\Sigma(k^3\chi_{exp})^2$. $Co^{3+} = N^{3+}_{Co}/(N^{3+}_{Co} + N^{2+}_{Co})$.

coordination numbers ($CN_{Mn\text{-}Me_1}$) from ~4.5 to ~5.2 because of the filling of vacancies by Co^{3+}. The relative variation of *CN* is 15%, which is significant. At the same time, the number of Co-Me pairs ($CN_{Co\text{-}Me_1}$) was found to decrease from ~4.6 to ~2.7 with increasing Co content despite the presence of 5–6 nearest Mn atoms around each vacancy (Table 5). These two contrasting trends appear to conflict and thus warrant some explanation. The apparent loss of Co neighbors across edges results from the multiplicity of Co sites and the property of EXAFS to average the different local environments. In the present situation, Co atoms are located either at the layer surface (corner links) or within Mn layers (edge links). EXAFS coordination numbers are a weighted average of the different crystallographic environments, so that a modification of the partitioning of Co atoms between these two sites results in an apparent loss or gain of coordination number. For example, Figure 7 and Table 5 show that the relative decrease in the number of edge-sharing Co-Mn pairs ($\langle CN\rangle^{Co}_{edge}$) at increasing loading is accompanied by an increase in the number of corner-linkages ($\langle CN\rangle^{Co}_{corner}$). Consequently, the opposite trends that are observed for the amplitudes of the edge-sharing peaks in the Mn and Co RSFs with increasing Co concentration simply indicate that $\langle CN\rangle^{Co}_{corner}$ increases faster than $\langle CN\rangle^{Co}_{edge}$. Thus, both Co and Mn *K*-edge measurements are consistent with an increase in the number of layer edge-sharing pairs at increasing Co concentration.

Quantitative analysis: Next-nearest (Co,Mn) shells. Co and Mn RSFs all display a third peak at ~3.1 Å (Fig. 6). This peak was repeatedly observed in various of manganese compounds (Friedl et al. 1997; Manceau and Charlet 1992; Manceau and Combes 1988; Silvester et al. 1997) and can either correspond to a side-lobe peak, originating from the limited reciprocal space integrated in the Fourier transform (i.e., a truncation effect), or it may be structural in origin. The first hypothesis can be discarded for several reasons. First, Manceau and Combes (1988) and Manceau (1995) showed that side lobes are best minimized by using a Kaiser window function, the side-lobe intensity being about 5% of the intensity of main structural peaks. Second, as shown by Silvester et al. (1997), this peak is absent in monoclinic birnessite, which has no corner linkages. If this peak at ~3 Å was a side lobe, it would be observed at the bottom of the huge edge-sharing second RSF peak even in the absence of corner links. Third, for a given Fourier-integration range, the ratio of intensities of the main and side-lobe peaks is constant. Thus, when main peaks in the RSF drop, their side lobes should drop in unison. Examination of Figure 6 shows that the intensities of the second and third RSF peaks are independent. A fourth argument can also be presented, which is based on the comparison with inverse Fourier transforms of the second and third RSF peaks, windowed together (Fig. 8c). If the third peak was a side lobe of the second one, the frequency of the resulting wave would be unique and close to that observed in Figure 8b where the second RSF peak was isolated. Comparison of Figures 8b and 8c demonstrates that the addition of the third peak of the RSFs in the Fourier transform produces a wave beating between 5 and 7 $Å^{-1}$. This beating is apparent even for S1, which has the weakest 3rd RSF peak, manifest in the form of similar amplitudes of the second and third oscillations. Last, according to XRD data (Chukhrov et al. 1985; Drits et al. 1997), hexagonal birnessite has interlayer cations above or below vacant sites located at ~3.4–3.5 Å from nearest layer Mn atoms. This crystallographic distance should yield an RSF peak at the phase-shift-uncorrected distance of ~3.1 Å. In conclusion, all these arguments solidly support a structural origin for the third peak in the RSFs often observed in phyllomanganate minerals (Manceau and Charlet 1992; Manceau and Combes 1988). In Co-sorbed samples, this peak can be

TABLE 5. EXAFS parameters for Co-(Mn,Co) and Mn-(Mn,Co) pairs and comparison with ⟨*CN*⟩ values obtained for a random distribution of layer and interlayer cations

		$Me\text{-}Me_{edge}$			$Me\text{-}Me_{corner}$			⟨*CN*⟩	
Sample	Atomic pair	*R* (Å)	$\langle CN\rangle_{edge}$	Δσ (Å)	*R* (Å)	$\langle CN\rangle_{edge}$	Δσ (Å)	$\langle CN\rangle_{edge}$	$\langle CN\rangle_{corner}$
HBi	Mn-Mn	2.86	4.1	0.00	3.49	2.0	0.03		
S1	Co-Mn	2.84	4.6	0.00	3.47	2.0	0.02	4.4	1.5
	Mn-Mn	2.86	4.5	0.01	3.48	1.7	0.02	4.7	1.2
S2	Co-Mn	2.83	3.3	0.00	3.50	2.5	0.02	3.3	2.5
	Mn-Mn	2.86	5.2	0.01	3.48	1.3	0.02	5.0	1.1
S3	Co-Mn	2.83	2.7	0.00	3.51	3.2	0.02	3.0	2.8
	Mn-Mn	2.86	5.2	0.01	3.48	1.0	0.01	5.1	1.0

Note: For all fits $Q \leq 0.02$.

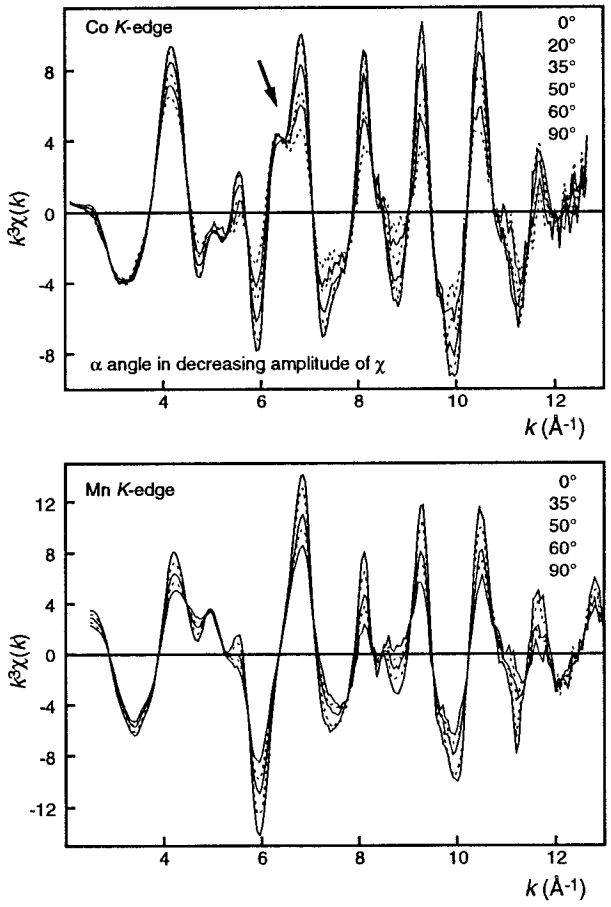

FIGURE 9. The k^3-weighted Co and Mn *K*-edge polarized EXAFS spectra for S2 at α angles of 0°, 20°, 35°, 50°, and 60°. The 90° spectra were calculated using the method described in the text. Note the presence of isosbestic points where, for a certain value of *k*, all $\chi(k,\alpha)$ functions are equal.

attributed to corner-linkages between Mn-Co octahedra as well as Mn-Mn octahedra.

The chemical nature of the corner linkages may be inferred from examination of Figure 8c. In fact, the effect on the Co-Me_2 wave frequency of introducing the third peak of the RSFs in the back Fourier transforms has a close parallel with results obtained for the first O shell analysis (compare Figs. 8a and 8c). In Figure 8c the intensity of the wave beating near 5–7 $Å^{-1}$ increases with Co loading and, consequently, with increasing Co^{2+}/Co^{3+} ratio. Because the increasing amount of Co^{2+} modifies only the contribution of corner links (Fig. 8c), and does not effect the edge links (Fig. 8b), it can be deduced that Co^{2+} octahedra bond birnessite layers by sharing corners. From S1 to S3, the number of Co-Me_2 pairs increases from 2.0 to 3.2 while the interatomic distance increases from 3.47 to 3.51 Å (Table 5). It will be shown later that this change of distance is due to a variation of the Co^{3+}/Co^{2+} ratio in the interlayer.

In conclusion, the analysis of powder EXAFS spectra shows that Co^{2+} bonds the layer surface exclusively by sharing corners with Mn octahedra and that Co^{3+} is present within the phyllomanganate layer. On the basis of the evidence presented thus far it is not possible to eliminate the possibility that Co^{3+} also occupies corner-sharing positions, in addition to edge-sharing positions in the layers. This point is important for understanding the oxidation mechanism of Co and is addressed next.

Polarized EXAFS

Co and Mn P-EXAFS spectra are displayed in Figure 9. Note the extremely high signal-to-noise ratio even at high *k* values. The presence of isosbestic points where, for a certain value of *k*, $\chi(k,\alpha)$ is independent of the experimental α angle provides a stringent test for the reliability of the measurements. All spectra must cross precisely at these specific *k* values, and a close examination of Figure 9 shows that this is the case up to at least 11 $Å^{-1}$. The *k*- and k^3-weighted RSFs derived from the $\chi(k,\alpha)$ spectra in Figure 9 are shown in Figure 10. This figure shows that all peaks in the RSF drop in amplitude when α is increased, which indicates that $\beta > 54.7°$ for all atomic pairs. This result is obvious for Mn-Mn_1 pairs ($\beta = 90°$) but it provides critical information about the oxidation state of sorbed Co atoms. It is reasonable to assume that β depends on the size of sorbed cations because the larger the ionic radii, the greater the Mn-Me distance and, consequently, the lower the β value. β should increase in the following order: Mn^{2+} (0.83 Å) < Zn^{2+} (0.74 Å) ≈ Co^{2+} (0.745 Å) < Mn^{3+} (0.645 Å) < Co^{3+} (0.545 Å) < Mn^{4+} (0.53 Å). Because $\beta = 53.5° \approx 54.7°$ in chalcophanite (Wadsley 1955; Post and Appleman 1988), it is likely that cations smaller than Zn would have a larger β value. Thus, a β value larger than 54.7° for the CoBi sample S2 points to the presence of Co^{3+} in the interlayer because for Co^{2+} the β angle is expected to be ~54.7°, as in chalcophanite. However, the presence of some Co^{2+} was undoubtedly identified from the analysis of powder spectra with increasing surface loading, which indicates the presence of both divalent and trivalent Co above layer vacancies. Additional support for a mixture of Co oxidation states comes from the quantitative analysis of P-EXAFS spectra.

Normalized numbers of nearest

$$[CN^{\alpha}_{(Mn,Co)\text{-}Me_1}/CN^{\alpha=0°}_{(Mn,Co)\text{-}Me_1}]$$

and next-nearest

$$[CN^{\alpha}_{(Mn,Co)\text{-}Me_2}/CN^{\alpha=0°}_{(Mn,Co)\text{-}Me_2}]$$

Mn,Co neighbors determined from least-squares fits are reported in Figure 11. Note that $CN^{\alpha=90°}_{Mn\text{-}Me_1}$ and $CN^{\alpha=90°}_{Co\text{-}Me_1}$ are not zero because of the partial disorientation of particles in the film plane. This disorientation can be quantified from the reduction of CN_{app} in going from $\alpha = 0°$ to $\alpha = 90°$, amounting to ~60% at the Co *K* edge and ~55% at the Mn *K* edge. These two values are in reasonably good agreement and are reinforced by the parallel nature of the $(CN^{\alpha}_{Mn\text{-}Me_1}/CN^{\alpha=0°}_{Mn\text{-}Me_1}) = f(\alpha)$ and $(CN^{\alpha}_{Co\text{-}Me_1}/CN^{\alpha=0°}_{Co\text{-}Me_1}) = f(\alpha)$

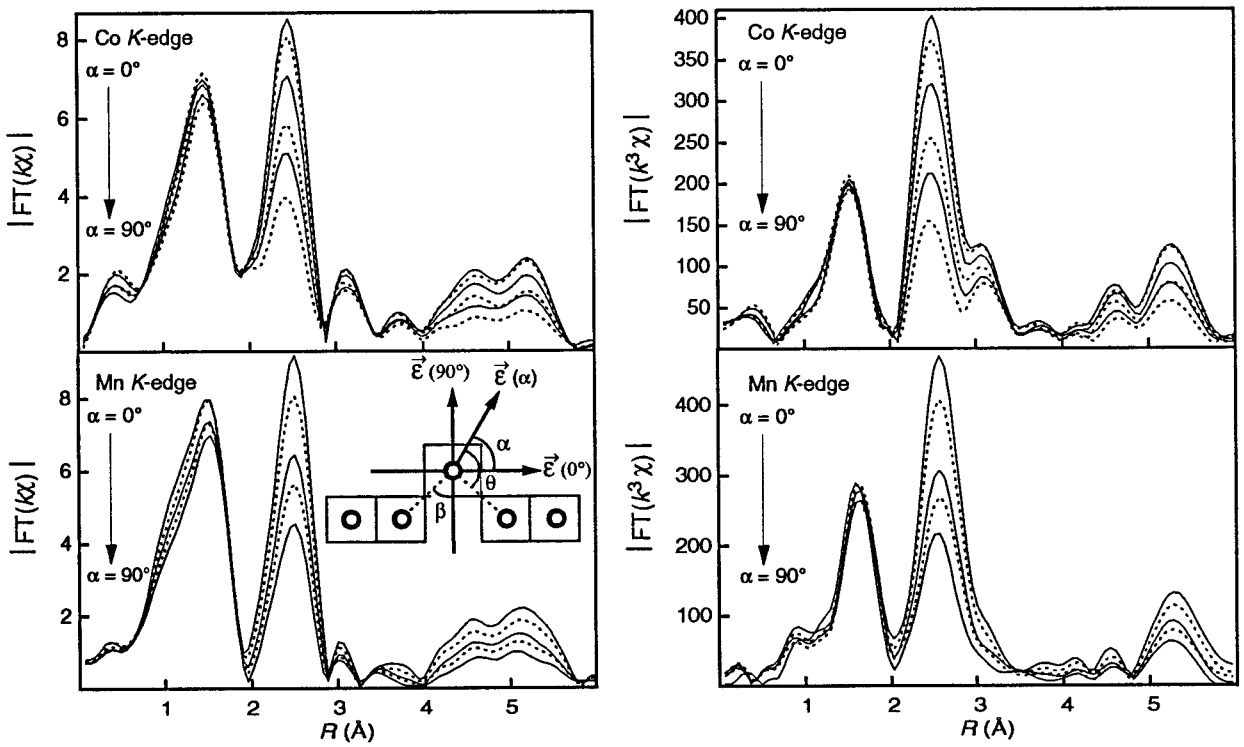

FIGURE 10. Co and Mn *K*-edge polarized RSFs for S2 at α angles of 0°, 20°, 35°, 50°, and 60° derived from the EXAFS spectra shown in Figure 12. The 90° spectra were calculated.

lines shown in Figure 11. The small difference can be attributed to some unidentified systematic errors. The magnitude of reduction of the third peak in the RSFs ($CN^{\alpha}_{Mn\text{-}Me_2}/CN^{\alpha=0°}_{Mn\text{-}Me_2}$ and $CN^{\alpha}_{Co\text{-}Me_2}/CN^{\alpha=0°}_{Co\text{-}Me_2}$) against α depends on two factors: the disorientation of particles and the β value, because $\beta \neq 90°$. The difference in slope between the $CN^{\alpha}_{Mn\text{-}Me_2}/CN^{\alpha=0°}_{Mn\text{-}Me_2} = f(\alpha)$ and $CN^{\alpha}_{Co\text{-}Me_2}/CN^{\alpha=0°}_{Co\text{-}Me_2} = f(\alpha)$ lines reflects the difference in β angle between the two pairs and hence provides information about the Mn^{3+} and Co atoms located at the layer surface. Since the radius of Mn^{3+} is larger than Co^{3+}, but the angular dependence of $CN^{\alpha}_{Co\text{-}Me_2}/CN^{\alpha=0°}_{Co\text{-}Me_2}$ less than that for $CN^{\alpha}_{Mn\text{-}Me_2}/CN^{\alpha=0°}_{Mn\text{-}Me_2}$ (Fig. 11), it must be concluded that both Co^{2+} and Co^{3+} are located above or below layer vacancy sites. Put another way, if only Co^{3+} were located at vacancy sites, the angular dependence of $CN^{\alpha}_{Co\text{-}Me_2}/CN^{\alpha=0°}_{Co\text{-}Me_2}$ would be greater than $CN^{\alpha}_{Mn\text{-}Me_2}/CN^{\alpha=0°}_{Mn\text{-}Me_2}$. Therefore we conclude that a mixture of Co^{2+} and Co^{3+} is adsorbed at layer vacancies.

It is concluded from this polarized EXAFS analysis that vacant sites are exclusively filled by trivalent Co, whereas external surface sites contain both Co^{2+} and Co^{3+}. A closer look at the EXAFS results shows that the relative amount of interlayer divalent and trivalent Co varies with the total Co concentration. Indeed, the Co-Me_2 distance was shown to increase from ~3.47 to ~3.51 Å with increasing Co concentration (Table 5). This variation is noticeable in the Co RSFs because the third peaks for S2 and S3 are shifted to longer distances relative to S1 (Fig. 7b). Associated with this peak shift is a progressive enhancement and broadening. The first effect is simply due to the increasing number of TC-sharing pairs, whereas the latter stems from the increasing contribution of Co^{2+}-Me_2 to the Co-Me_2 peak at increased Co loading. Thus, one may deduce that, unlike S1 which has no or very little Co^{2+}, the interlayers of S2 and S3 contain both Co^{2+} and Co^{3+} cations.

We have seen in Figure 5 that with increased Co loading, the shoulder at 6.3 $Å^{-1}$ is reinforced at the expense of the main oscillation at 6.8 $Å^{-1}$ (see arrows). The same spectral evolution is observed for S2 with increasing α angle (Fig. 9, arrows) due to the increased weighting of the corner-sharing contribution relative to edge sharing. This structural interpretation is further reinforced by the $\langle CN\rangle^{Co}_{corner}/\langle CN\rangle^{Co}_{edge}$ values, which increase from 0.3 for S1 to 1.2 for S3 (Table 5). Thus, we may conclude that the frequency that peaks at 6.3 $Å^{-1}$ is characteristic of corner-sharing octahedra, and the frequency that peaks at 6.8 $Å^{-1}$ is characteristic of edge-sharing octahedra.

DISCUSSION

Chemical composition for Co-sorbed birnessite

Sample S1. The average chemical composition of S1 can be determined from the combination of chemical analysis, EXAFS, and XRD data. According to EXAFS, almost all Co in S1 is trivalent and located predominantly, if not entirely, within layers. Indirect evi-

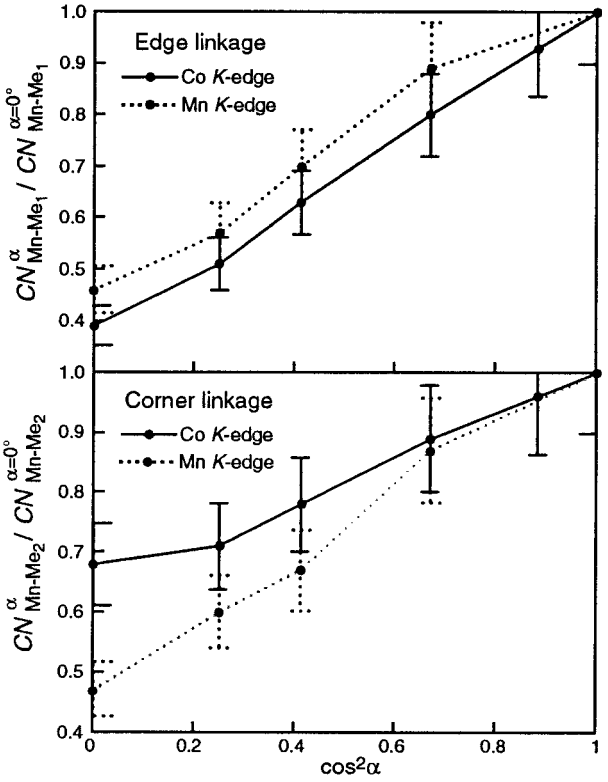

FIGURE 11. Number of nearest and next-nearest Mn,Co neighbors as a function of $\cos^2\alpha$ for S2.

dence for the existence of Co^{3+} atoms in vacant sites comes from the simulation of XRD patterns, which showed that the density of vacant sites, $CN_{\square}$, decreased from 0.17 in HBi (Silvester et al. 1997) to 0.11 in S1. The fraction of interlayer cations N_{IC} was found to decrease by the same amount, which indicates that the filling of vacant sites occurs at the expense TC-sharing cations. Interestingly, this variation of the layer and interlayer site occupancies matches precisely the proportion of Co atoms in the solid as determined by chemical analysis (Co/Mn = 0.05). Thus, the combination of chemical analysis and XRD simulations provides additional support for the migration of Co^{3+} to vacant sites. If one assumes that all divalent Co is oxidized by trivalent Mn (this hypothesis is discussed later), then the total number of trivalent cations remains the same as in HBi (i.e., 0.21 cations per octahedron), and the chemical composition for S1 can be written: $Mn^{2+}_{0.06}Mn^{3+}_{0.05}Co^{3+}_{0.01}(Mn^{4+}_{0.74}Mn^{3+}_{0.10}Co^{3+}_{0.05}\square_{0.11})O_{1.71}(OH)_{0.29}$. Examination of this chemical formula leads to the following remarks. (1) S1 and HBi have the same anion composition. Thus, interlayer Na cations of the initial NaBu are completely replaced by protons, the same as Co-free HBi (Drits et al. 1997; Silvester et al. 1997). (2) The amount of Co^{3+} in layers (5%) corresponds to the amount of vacant sites initially formed during the low-pH equilibration resulting from the rapid disproportionation of layer Mn^{3+} according to $2Mn^{3+} \rightarrow Mn^{4+} + Mn^{2+}$. In addition, the presence of 0.05 Co^{3+} in layers is accompanied by a decrease of the same amount of interlayer Mn^{3+}.

Assuming a random mixing of Co and Mn atoms within the layers and the interlayers it is possible to calculate $\langle CN\rangle^{Mn,Co}_{edge}$ and $\langle CN\rangle^{Mn,Co}_{corner}$ from the chemical composition of S1. These values can be compared with those determined from the quantitative EXAFS analysis. The number of atomic neighbors determined by EXAFS is a weighted average of the different environments: $\langle CN\rangle = \Sigma_i W_i CN_i$, where i refers to the different sites of a given element, W_i is the site occupancy of the element, and CN_i is its number of neighbors at site i. From the chemical composition of S1 we calculate

$$\langle CN\rangle^{Co}_{edge} = \frac{0.05}{0.06}(0.89 \times 6) = 4.4,$$

$$\langle CN\rangle^{Co}_{corner} = \frac{0.05}{0.06}(0.12 \times 6) + \frac{0.01}{0.06}5.34 = 1.5,$$

$$\langle CN\rangle^{Mn}_{edge} = \frac{0.84}{0.95}5.34 = 4.7, \quad \text{and}$$

$$\langle CN\rangle^{Mn}_{corner} = \frac{0.84}{0.95}0.72 + \frac{0.11}{0.95}5.34 = 1.2.$$

These values compare well with those determined from the quantitative EXAFS analysis (Table 5). It should be emphasized that this agreement simply confirms the consistency of this chemical formula with EXAFS data and does not exclude the possible existence of a particular Co and Mn ordering, which could also give a good agreement. The question of the distribution of Mn and Co cations within birnessite layers is addressed later.

Samples S2 and S3. CN_{IC}, $CN_{\square}$, $Co^{3+}/(Co^{3+} + Co^{2+})$, and Co/Mn are known from XRD, EXAFS, and chemical analysis. Thus, if we again assume that the total number of trivalent cations is the same as in HBi, then their average cation composition can be written in the general form:

$$(Mn^{2+}, Co^{2+})_{CN_{IC}-CN_{\square}+0.05}(Mn^{3+}, Co^{3+})_{CN_{\square}-0.05}\text{-}$$
$$[Mn^{4+}_{0.74}(Mn^{3+}, Co^{3+})_{0.26-CN_{\square}}\square_{CN_{\square}}] \quad (4)$$

The value 0.05 arises from the initial disproportionation of 0.1 Mn^{3+} per octahedron. For S2, $CN_{IC} = 0.12$, $CN_{\square} = 0.10$, $Co^{3+}/(Co^{3+} + Co^{2+}) = 0.8$, and Co/Mn = 0.14, and formula 4 can be written as $(Mn^{2+},Co^{2+})_{0.07}(Mn^{3+}, Co^{3+})_{0.05}[Mn^{4+}_{0.74}(Mn^{3+},Co^{3+})_{0.16}\square_{0.10}]O_{1.73}(OH)_{0.27}$ or $Mn^{2+}_{0.07-x}$-$Co^{2+}_{x}Mn^{3+}_{0.05-y}Co^{3+}_{y}(Mn^{4+}_{0.74}Mn^{3+}_{0.16-z}Co^{3+}_{z}\square_{0.10})O_{1.73}(OH)_{0.27}$ because $(y + z)/(x + y + z) = 0.8$ and $(x + y + z) = 0.14$ $(1.02 - x - y - z)$ we have $x = 0.25\ (y + z)$; $x + y + z = 0.125$; $(y + z) = 0.100$; $z = 0.100 - y$ and $Mn^{2+}_{0.04}Co^{2+}_{0.03}Mn^{3+}_{0.05-y}Co^{3+}_{y}(Mn^{4+}_{0.74}Mn^{3+}_{0.06+y}Co^{3+}_{0.10-y}\square_{0.10})O_{1.73}$-$(OH)_{0.27}$ where y has been optimized to obtain a good agreement with the number of Mn-Mn and Mn-Co edge- and corner-sharing octahedra determined by EXAFS (Table 5). The average chemical composition for S2 can be

finally expressed as: $Mn^{2+}_{0.04}Co^{2+}_{0.03}Mn^{3+}_{0.03}Co^{3+}_{0.02}(Mn^{4+}_{0.74}Mn^{3+}_{0.08}Co^{3+}_{0.08}\square_{0.10})O_{1.73}(OH)_{0.27}$.

For S3, $CN_{IC} = 0.13$, $CN_{\square} = 0.10$, $Co^{3+}/(Co^{3+} + Co^{2+}) = 0.7$, and Co/Mn = 0.24, and the set of possible chemical formulae is: $Mn^{2+}_{0.02}Co^{2+}_{0.06}Mn^{3+}_{0.05-y}Co^{3+}_{y}(Mn^{4+}_{0.74}Mn^{3+}_{0.02+y}Co^{3+}_{0.14-y}\square_{0.10})O_{1.75}(OH)_{0.25}$. $y = 0.03$ and $y = 0.04$ values give very similar $\langle CN\rangle^{Mn,Co}_{edge}$ and $\langle CN\rangle^{Mn,Co}_{corner}$ values, which are both in fair agreement with EXAFS results considering a precision of ~10%. The average chemical composition for S3 can be written: $Mn^{2+}_{0.02}Co^{2+}_{0.06}Mn^{3+}_{0.02}Co^{3+}_{0.03}(Mn^{4+}_{0.74}Mn^{3+}_{0.05}Co^{3+}_{0.11}\square_{0.10})O_{1.75}(OH)_{0.25}$.

Comparison of the chemical formulae for HBi, S1, S2, and S3 leads to the following remarks.

(1) In spite of the small variation of CN_{IC} (0.12–0.13), the chemical composition of the interlayer changes markedly with increasing Co sorption, with $Co^{3+}_{interlayer}$ tending to substitute for $Mn^{3+}_{interlayer}$ and $Co^{2+}_{interlayer}$ for $Mn^{2+}_{interlayer}$. The same trend is observed for trivalent layer cations.

(2) The amount of interlayer protons decreases with increasing Co concentration. In S1 the layer charge is balanced equally by interlayer cations (0.30) and protons (0.29), as in the case of HBi, whereas in S3 the layer charge is mainly compensated by interlayer cations (0.31 vs. 0.25). The decrease in the amount of protons is due to the formation of pairs of TC octahedra above and below vacant sites, because for S2 and S3 the number of interlayer cations is greater than the number of vacancies (0.12–0.13 vs. 0.10). The bonding of interlayer metal ions to undersaturated surface O atoms at vacant sites logically leads to the departure of protons, for charge-balance reasons.

(3) The *a* parameter is reduced significantly in S1 (2.838 Å) compared with HBi (2.848 Å), but with increasing Co content it increases slightly to 2.840 Å (S2) and 2.842 Å (S3). These changes can be understood by considering the modifications that occur to the layer and interlayer chemical compositions. Three scenarios can be envisaged. First, the decrease in the density of vacancies from 0.11 (S1) to 0.10 (S2, S3) increases the electrostatic repulsion between layer cations, which could increase the *a* parameter for S2 and S3 compared with S1. This hypothesis can be rejected because the opposite trend is observed between HBi and S1, where a decrease in the density of vacancies from 0.17 to 0.11 leads to a decrease in the *a* parameter by 0.01 Å. The second alternative is that the replacement of Mn^{3+}_{layer} by the smaller Co^{3+}_{layer} cation contributes to a decrease in *a*, but this interpretation is not consistent with the increase of *a* in S3 compared with S1 because the former contains more Co^{3+}_{layer}. The third explanation is related to the amount, and nature, of interlayer cations and their distribution around vacant sites. It is reasonable to suppose that the presence of cations above and below vacant octahedra increases the lateral size of these sites: The more interlayer cations the higher the *a* parameter. For example, the strong decrease in the amount of interlayer cations in S1 comparison with HBi leads to a decrease in the *a* parameter (2.848 vs. 2.838 Å). The dependence of *a* on the interlayer occupancy is more pronounced when cations are located above and below vacant sites. In going from S1 to S3, the percentage of vacancies that have pairs of TC-sharing cations increases from 10% (S1), to 20% (S2), and to 30% (S3), and this evolution is accompanied by an increase in the *a* parameter (2.838–2.842 Å). Additional support for this interpretation is provided by the structure of chalcophanite. The layers of chalcophanite contain only Mn^{4+}. One in every seven layer cation sites is vacant, with pairs of TC-sharing Zn^{2+} octahedra located above and below (Fig. 1). As a consequence, chalcophanite has a relatively large *a* parameter of 2.850 Å (based on an hexagonal layer symmetry) in comparison with CoBi.

(4) With increased Co loading the proportion of Co^{2+} (of total Co) increases while the proportion of Mn^{3+} (of total Mn) decreases. As a consequence, at high Co loading the valency mixture of Co is greater, while that for Mn is lower. This accounts for the observed lower intensity of the Co-O peak in Co RSFs and the corresponding higher intensity of the Mn-O peak in Mn RSFs with increased Co concentration (Fig. 5). This trend is confirmed by the quantitative treatment of EXAFS data, with an increase of $\langle CN_{Mn\text{-}O}\rangle$ from 4.2 (S1) to 5.3 (S3) and the splitting of the Co-O shell into one Co^{3+}-O and one Co^{2+}-O sub-shell (Table 4). This agreement between EXAFS and chemical compositions supports the hypothesis of oxidation of Co^{2+} by Mn^{3+}.

Structural transformation of Na-exchanged buserite to Co-sorbed birnessite

Structural models for the oxidation of Co. In the absence of Co, the low-pH weathering of NaBu strongly alters its structure (Fig. 2). Two major transformations have been identified (Drits et al. 1997; Silvester et al. 1997). Na is exchanged by H^+ and 0.1 Mn^{3+} per octahedron disproportionate to form vacancies and solution Mn^{2+}, the latter of which then re-adsorb above and below vacancies. This transformation is associated with a migration of ~50% of the remaining Mn^{3+}_{layer} to the interlayer space, accounting for the monoclinic-to-hexagonal birnessite conversion. This sequence of structural transformations is shown schematically in Figure 2 for microcrystallites of type II, which possess a constant and well-defined stoichiometry.

In the present study, Co and NaBu were added simultaneously and then equilibrated at pH 4. Consequently, the weathering of NaBu and the sorption of Co occurred concurrently. Analysis of the chemical formulae of the CoBi prepared in this study leads to the following remarks. First, Co-sorbed samples and HBi have a similar anion and proton composition ($1.70 < O < 1.75$; $0.25 < OH < 0.30$). The H^+ content is nearly equal to the amount of interlayer Na originally present in NaBu (0.30), which means that the mechanism of Na^+ desorption and H^+ adsorption was not perturbed by the presence of Co, at least at low Co concentration. Stated another way, the adsorption and oxidation of Co^{2+} at the buserite surface interfered with, but did not prevent, the exchange of interlayer

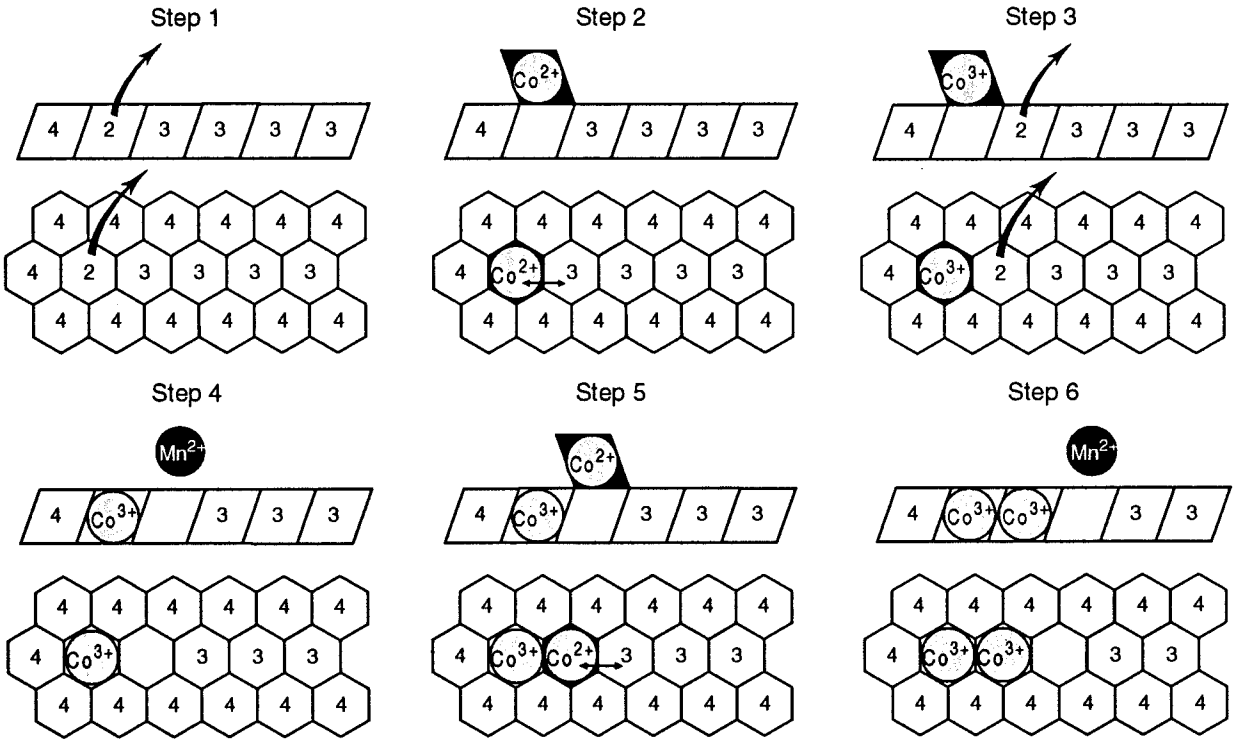

FIGURE 12. First mechanism (M1) for the oxidation of Co^{2+} to Co^{3+} at the HBi-water interface. For each step, structural units are projected in the *a-b* and *b-c* plane. This latter projection is cut along an Mn^{3+}-rich row. Arabic numbers correspond to the oxidation state of Mn. In step 2, an electron is transferred from Co^{2+} to Mn^{3+}, and the reduced Mn^{2+} leaves the layer in step 3. Steps 5 and 6 are replicates of steps 2 to 4.

Na for protons at low pH. Second, all CoBi samples contain large amounts of vacant sites in the layers. For S1 the sum of layer Co and vacancies equals the amount of vacancies in HBi (0.167), and for S2 and S3 this sum is even slightly higher (0.18–0.21). This important result suggests that the filling of layer vacancies by Co^{3+} does not modify the vacancy formation mechanism associated with the monoclinic buserite to the hexagonal birnessite conversion (i.e., disproportionation and migration of layer Mn^{3+}).

From these general observations, two structural mechanisms can be envisaged for the oxidation of Co^{2+} (Figs. 12 and 13). In the first mechanism (M1), $Co^{2+}_{solution}$ sorbs onto vacant sites created as a result of the fast Mn^{3+} disproportionation (steps 1–2, Fig. 12). The sorbed Co^{2+} is then oxidized by the nearest layer Mn^{3+}, which is reduced to Mn^{2+} (step 3). The newly formed interlayer Co^{3+} migrates into the underlying vacant site while the adjacent Mn^{2+} moves out of the layer, into either solution or an interlayer position (step 4). This Co^{3+}_{layer} is then surrounded by five Mn^{4+} and one vacancy. The oxidation process may end at this point, but the sorption of a new $Co^{2+}_{solution}$ and its further oxidation by the next Mn^{3+} along the Mn^{3+}-rich row seems feasible (steps 4–5). Thus, this mechanism may be replicated along a Mn^{3+}-rich row as long as a sorbed Co^{2+} has an adjacent Mn^{3+}. Ultimately this mechanism results in the formation of short $Mn^{4+}Co^{3+}Co^{3+}\ldots\square$ chains, in place of the former Mn^{3+} rows.

This oxidation process has several important consequences that deserve to be outlined. First, since Co^{3+}_{layer} cations are only surrounded by Mn^{4+} and Co^{3+}, the five to six Co-(Mn,Co) distances should be identical. This high structural ordering should lower the EXAFS Debye-Waller factor and, accordingly, enhance the electronic wave amplitude associated with this nearest cationic shell contribution. Second, because Co atoms contain more electrons than Mn atoms, the possible existence of Co-Co pairs may contribute to a further enhancement of the wave amplitude. This mechanism therefore provides an explanation of the notable increase in amplitude of the second peak in the Co RSFs relative to the equivalent peak in the Mn RSFs that is consistently observed in natural and synthetic Co-containing phyllomanganates (Fig. 6). Third, mechanism 1 also accounts for the reduction of the Co^{3+}_{layer}-$(Mn^{4+},Co^{3+})_{layer}$ distance in comparison with Mn_{layer}-$(Mn^{3+/4+},Co^{3+})_{layer}$ (2.83–2.84 Å vs. 2.86 Å, Table 5) because Co^{3+}_{layer} is surrounded on average by nearest cations smaller than Mn_{layer}.

The second mechanism (M2), schematically drawn in Figure 13, considers the possibility that the sorption of solution Co^{2+} occurs after the structural transformation of NaBu to HBi is complete (step 1). In this mechanism, solution Co^{2+} is oxidized by $Mn^{3+}_{interlayer}$, and the resulting

Mn^{2+} either enters into the solution or sorbs onto vacant sites (step 2). Three different cation ordering sequences along *b* can be created depending on the local chemical surroundings of $Co^{3+}_{interlayer}$. They are: Mn^{4+}_{layer}-$Co^{3+}_{interlayer}$-Mn^{3+}_{layer}, □-$Co^{3+}_{interlayer}$-Mn^{3+}_{layer}, or Mn^{3+}_{layer}-$Co^{3+}_{interlayer}$-Mn^{3+}_{layer}. As for M1, it is envisaged that $Co^{3+}_{interlayer}$ migrates into the underlying vacant site in the two first situations (step 3). In the third case, however, Co^{3+} migration is unlikely because this results in the formation of Mn^{3+}_{layer}-Co^{3+}_{layer}-Mn^{3+}_{layer} sequences that are sterically unfavorable. This proposition is supported by comparison with the Co-free buserite and birnessite structures in which Mn^{4+} and Mn^{3+} atoms do not mix at random but form Mn^{4+}-rich and Mn^{3+}-rich rows along *b* (Fig. 1). Although some Mn^{4+} appears in the Mn^{3+}-rich rows it is not distributed randomly, but is instead always adjacent to a vacant site (Mn^{3+}_{layer}-Mn^{4+}_{layer}-□-Mn^{3+}_{layer} sequences). Because Co^{3+} and Mn^{4+} ions have identical ionic radii and a similar electronic configuration ($3d^6$ vs. $3d^3$, empty e_g orbitals) it is likely that they behave similarly and, in particular, avoid mixing with Mn^{3+} at the atomic scale. If $Co^{3+}_{interlayer}$ in a Mn^{3+}_{layer}-□-Mn^{3+}_{layer} sequence were to migrate into the underlying vacant site, it would be surrounded by four Mn^{4+} and two Mn^{3+} atoms. This structural environment is sterically unfavorable due to both the different sizes of Mn^{4+} and Mn^{3+} ions and the Jahn-Teller distortion of trivalent Mn octahedra. This structural environment is contrary to the observed enhancement of the edge-sharing Co-Mn EXAFS contribution in Co^{2+}-free samples (i.e., S1, asbolane, lithiophorite).

The juxtaposition of these two mechanisms, M1 and M2, with the chemical formulae of CoBi shows that neither can individually account for the oxidation of divalent Co. Each has its own merit and limitations. For instance, the second mechanism can account for the decrease in the amount of vacancies with increasing Co loading and for the presence of $Co^{3+}_{interlayer}$ and Co^{3+}_{layer} species, but the number of edge-sharing Co^{3+}_{layer} allowed by this process is low due to the high probability of having Mn^{3+}_{layer}-$Co^{3+}_{interlayer}$-Mn^{3+}_{layer} sequences. This mechanism could never allow for twice as many Co^{3+}_{layer} as Mn^{3+}_{layer}, as is observed for S3 ($Co^{3+}_{layer}/Mn^{3+}_{layer}$ = 0.11/0.05). On the other hand, the first mechanism allows the accumulation of large amounts of Co^{3+}_{layer} but provides no explanation for the existence of interlayer Co^{3+}. In addition, this mechanism maintains a constant density of vacant sites with increased Co loading.

Structural models and oxidation mechanism of Co on sorption samples. The two mechanistic models M1 and M2, presented in the previous section, do allow an understanding of the mechanism of Co oxidation on the different CoBi samples and enables the formation of realistic structural models that account for the whole set of structural and chemical data. To achieve these goals, models M1 and M2 must be applied to stoichiometrically well-defined initial solids. For this reason, the discussion uses type II microcrystallites (Fig. 2). Due to the mixing of crystallites I and II in bulk samples, only average

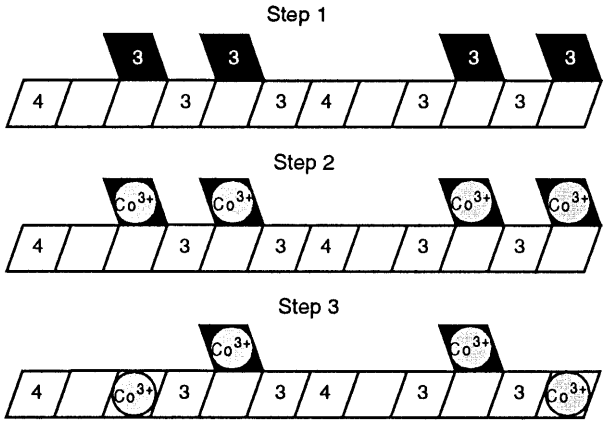

FIGURE 13. Second mechanism (M2) for the oxidation of Co^{2+} to Co^{3+} at the HBi-water interface. Projection in the *b*-*c* plane at the level of an Mn^{3+}-rich row. Co^{2+} is oxidized and replaces an interlayer Mn^{3+} (step 2). Its further migration to the manganate layer depends on the local environment. It is favorable whenever Co^{3+} is surrounded by a layer vacancy or Mn^{4+} and forbidden when it is surrounded by two Mn^{3+}.

chemical formulae are experimentally accessible, so that the cationic composition of Co-sorbed crystallites of type II cannot be known precisely. Fortunately, owing to the overwhelming predominance of type II microcrystallites in the bulk sample, their chemical composition is close to the bulk values. In any case, their structural formulae can be reasonably inferred from some simple considerations. First, NaBu crystallites II [$Na_{0.333}(Mn^{4+}_{0.667}Mn^{3+}_{0.333})O_{\sim 2}$] contain 2% more Mn^{3+} than the sample average [$Na_{0.30}(Mn^{4+}_{0.69}Mn^{3+}_{0.31})O_{\sim 2}$]. Consequently, type II particles should be more reactive and should be enriched in Mn^{3+}_{layer}, Co^{3+}_{layer}, and $Mn^{2+}_{interlayer}$ in comparison with type I particles and the average chemical composition. Second, because Co^{2+} is oxidized by Mn^{3+}, the total amount of trivalent cations in type II CoBi samples should be the same as in type II HBi crystallites (0.22, Fig. 2). On this basis, the chemical formulae of the three type II CoBi are:

$$S1_{II}: \quad Mn^{2+}_{0.07}Mn^{3+}_{0.04}Co^{3+}_{0.01}\text{-}(Mn^{4+}_{0.72}Mn^{3+}_{0.11}Co^{3+}_{0.06}\square_{0.11})O_{1.68}(OH)_{0.32}$$

$$S2_{II}: \quad Mn^{2+}_{0.05}Co^{2+}_{0.03}Mn^{3+}_{0.02}Co^{3+}_{0.02}\text{-}(Mn^{4+}_{0.72}Mn^{3+}_{0.09}Co^{3+}_{0.09}\square_{0.10})O_{1.70}(OH)_{0.30}$$

$$S3_{II}: \quad Mn^{2+}_{0.03}Co^{2+}_{0.06}Mn^{3+}_{0.01}Co^{3+}_{0.03}\text{-}(Mn^{4+}_{0.72}Mn^{3+}_{0.06}Co^{3+}_{0.12}\square_{0.10})O_{1.72}(OH)_{0.28}$$

These chemical formulae are close to those calculated on an average basis, keeping in mind that the precision on the cation site occupancy is estimated to be 0.01. This inherent uncertainty in the exact chemical composition of type II Co-containing crystallites is acceptable for describing the general oxidation pathway of Co as well as

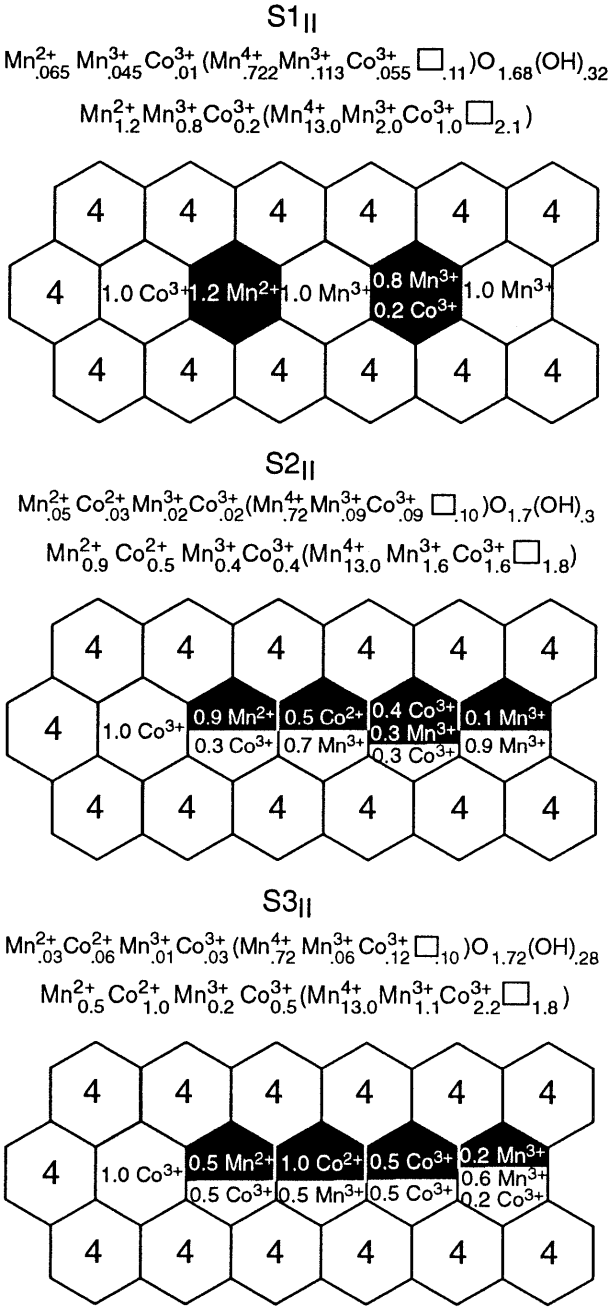

FIGURE 14. Idealized structure of type II microcrystallites for S1, S2, and S3. Structural formulae are written on a per-octahedron basis and for the half super-cell. Projection in the *a-b* plane. Interlayer octahedra are solid, and arabic numbers correspond to the oxidation state of Mn atoms.

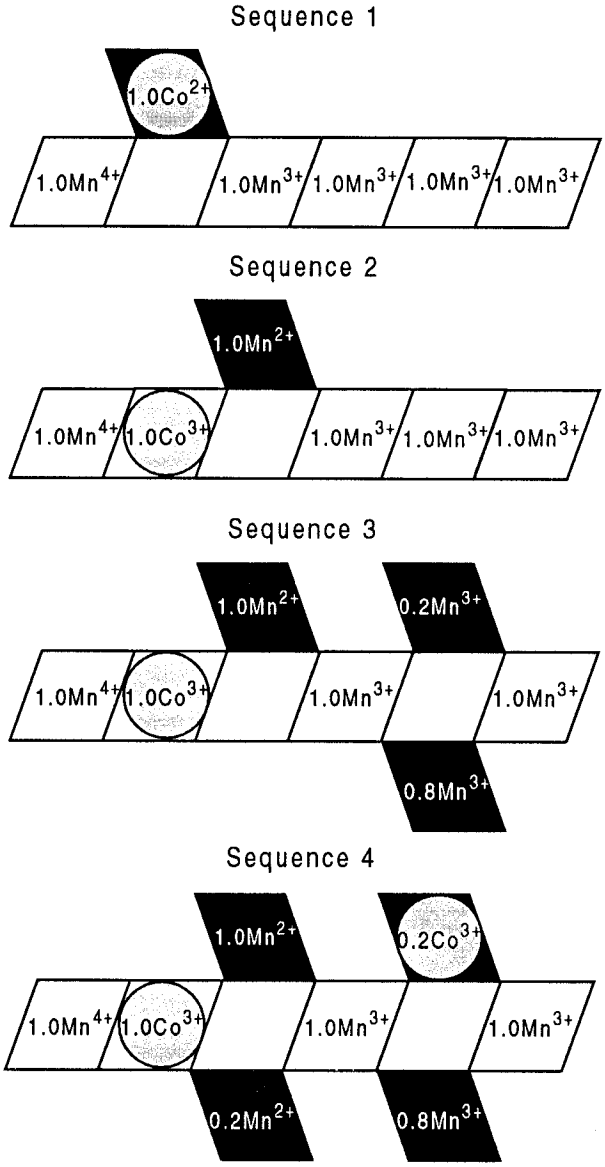

FIGURE 15. Schematic structural representation in the *a-b* plane of the oxidation of Co^{2+} to Co^{3+} on type II microcrystallites for S1. Seq. 1 = Sorption of $Co^{2+}_{solution}$; Seq. 2 = Oxidation and migration of $Co^{2+}_{interlayer}$ according to mechanism M1; Seq. 3 = migration of Mn^{3+}_{layer} to interlayer site. Seq. 4 = sorption of $Mn^{2+}_{solution}$ and $Co^{2+}_{solution}$ and oxidation of $Co^{2+}_{solution}$ by $Mn^{3+}_{interlayer}$ according to mechanism M2.

allowing sufficiently accurate structural models of the different CoBi end-products.

***S1*$_{II}$.** These particles contain little $Co^{3+}_{interlayer}$ and the amount of Co^{3+}_{layer} per octahedron (6%) is equal, within the precision of the site occupancy evaluation (~0.01), to the amount of vacant sites formed during the initial disproportionation step in the conversion of NaBu to HBi at low pH (5.5%). Consequently, Co^{2+} that is converted to Co^{3+}_{layer} is in all likelihood oxidized by Mn^{3+}_{layer} (first mechanism), and Co^{2+} that becomes $Co^{3+}_{interlayer}$ is oxidized by $Mn^{3+}_{interlayer}$ (second mechanism). A structural model for the half super-cell of $S1_{II}$ CoBi, which satisfies all crystal chemical requirements stated previously, is drawn in Figure 14. A structural description of the type II NaBu to $S1_{II}$ transformation is shown in Figure 15. The suite of chemical reactions corresponding to this structural transformation are listed below. Comments

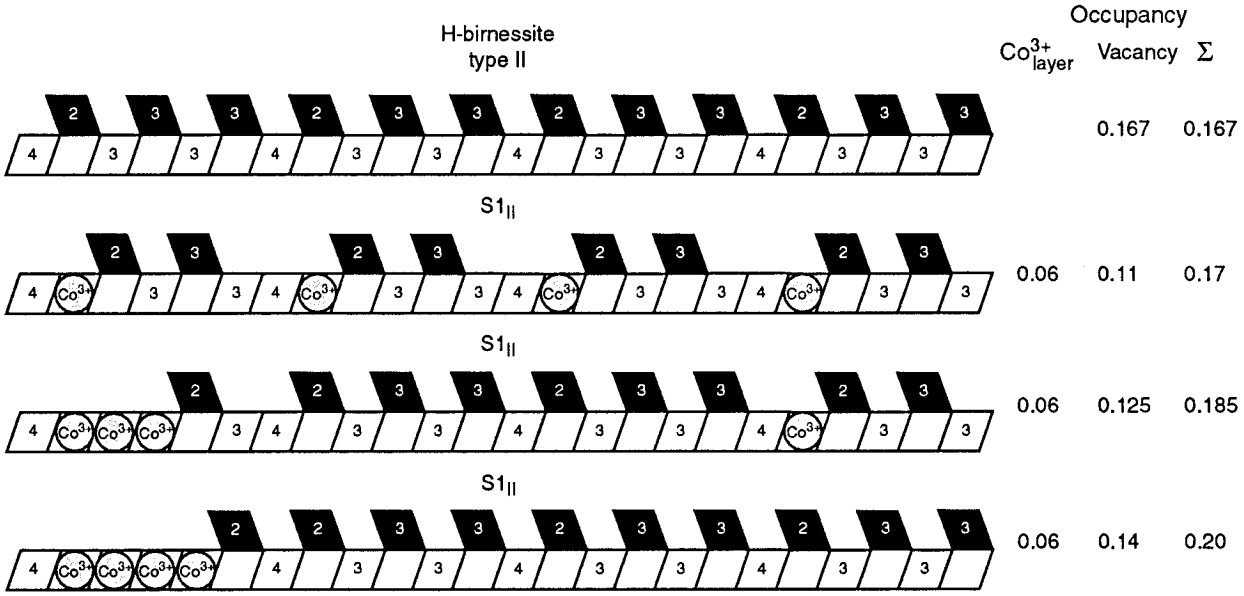

FIGURE 16. Idealized structural representation of $(Mn,Co)^{3+}$-rich rows in type II microcrystallites for S1 (*b*-*c* projection).

written above the arrows correspond to step numbers in Figure 12 for M1 and Figure 13 for M2, while comments below the arrows refer to the sequential steps shown in Figure 15. The reactions are:

$$Na_{0.333}(Mn^{4+}_{0.667}Mn^{3+}_{0.333})O_2 + 0.33\,H^+ + 0.065\,Co^{2+}$$

$$\xrightarrow[\text{seq1}]{\text{M1-step2}} Co^{2+}_{0.055}(Mn^{4+}_{0.722}Mn^{3+}_{0.223}\square_{0.055})O_{1.67}(OH)_{0.33}$$

$$+ 0.055\,Mn^{2+} + 0.01\,Co^{2+} + 0.333\,Na$$

$$\xrightarrow[\text{seq2}]{\text{M1-step3-4}} Mn^{2+}_{0.055}(Mn^{4+}_{0.722}Mn^{3+}_{0.168}Co^{3+}_{0.055}\square_{0.055})O_{1.67}(OH)_{0.33}$$

$$+ 0.055\,Mn^{2+} + 0.01\,Co^{2+} + 0.333\,Na$$

$$\xrightarrow[\text{seq3}]{\text{M2-step1}} Mn^{2+}_{0.055}Mn^{3+}_{0.055}(Mn^{4+}_{0.722}Mn^{3+}_{0.113}Co^{3+}_{0.055}\square_{0.11})O_{1.67}\text{-}$$

$$(OH)_{0.33} + 0.055\,Mn^{2+} + 0.01\,Co^{2+} + 0.333\,Na$$

$$\xrightarrow[\text{seq4}]{\text{M2-step2}} Mn^{2+}_{0.065}Mn^{3+}_{0.045}Co^{3+}_{0.01}(Mn^{4+}_{0.722}Mn^{3+}_{0.113}Co^{3+}_{0.055}\square_{0.11})\text{-}$$

$$O_{1.67}(OH)_{0.33} + 0.045\,Mn^{2+} + 0.333\,Na$$

For this structural model, $\langle CN\rangle^{Co}_{edge} = 4.2$, $\langle CN\rangle^{Co}_{corner} = 2.0$, $\langle CN\rangle^{Mn}_{edge} = 4.3$, and $\langle CN\rangle^{Mn}_{edge} = 1.7$. These values compare well with those determined from the quantitative EXAFS analysis (Table 5). However, this agreement is not very discriminating because similar values were obtained by assuming a random mixing of Mn and Co atoms in microcrystallites I and II ($\langle CN\rangle^{Co}_{edge} = 4.4$, $\langle CN\rangle^{Co}_{corner} = 1.4$). This is a consequence of the similarity of local environments for Mn and Co atoms in the two models and in the two types of crystals. Consequently, EXAFS spectroscopy provides direct evidence for the oxidation and migration of Co into buserite layers, but has little sensitivity to the relative distribution of Mn and Co atoms in the layers.

The possibility of mechanism 1 replicating along the Mn^{3+}-rich rows, as described in Figure 12, cannot be excluded a priori and needs to be addressed. An idealized representation of the structure of $(Mn,Co)^{3+}$-rich rows in HBi and CoBi is drawn in Figure 16. This figure shows that in the case where replication of mechanism 1 occurs, the result is both a clustering of Co^{3+}_{layer} and an increase of the vacancy density. In $S1_{II}$, the total number of Co^{3+}_{layer} plus vacant sites equals that in HBi (0.17), and consideration of Figure 16 shows that this condition is fulfilled where Co^{3+}_{layer} atoms are isolated. We may conclude that replication of mechanism 1 does not occur in $S1_{II}$ and that Co^{3+}_{layer} cations are diluted in the layers. Additional support for this structural interpretation is provided by EXAFS and XRD. First, if Co atoms were clustered in domains, their local structure would be similar to that of CoOOH, which, as discussed previously, is not supported by the EXAFS analysis. Second, the clustering of Co atoms in a few domains separated by large Co-free HBi areas is incompatible with the strong reduction of the layer parameter from 2.848 to 2.838 Å.

***S2*$_{II}$.** The presence of Co^{3+}_{layer} and $Co^{3+}_{interlayer}$ in $S2_{II}$ indicates that both mechanisms 1 and 2 occurred. In contrast with $S1_{II}$, the amount of Co^{3+}_{layer} is greater than the initial amount of vacancies created by the rapid disproportionation of Mn^{3+}_{layer} (5.5%). This additional amount of Co^{3+}_{layer} is either a result of the replication capacity of M1 (Fig. 12) or from the migration of $Co^{3+}_{interlayer}$ originating from M2 into vacant sites (Fig. 13). In fact, it proved impossible to build acceptable structural for-

mulae for $S2_{II}$ or $S3_{II}$ based on M1 alone. Indeed, even in the most realistic models, one is left with $Co^{2+}_{interlayer}$-Mn^{3+}_{layer} pairs or Mn^{3+}_{layer}-$Co^{3+}_{interlayer}$-Mn^{4+}_{layer} sequences, which are not likely for thermodynamic and crystal chemical reasons, respectively. In the former case interlayer Co^{2+} should be oxidized by the adjacent Mn^{3+}_{layer}, and in the latter it should migrate to the underlying vacant site. In addition, the assumption that M1 dominates is equivalent to assuming that the formation of $Mn^{4+}Co^{3+}Co^{3+}\ldots\square$ sequences is faster than the $Mn^{3+}_{layer} \rightarrow Mn^{3+}_{interlayer} \rightarrow Co^{3+}_{interlayer} \rightarrow Co^{3+}_{layer}$ reaction (M2). This is hardly tenable because the result would be the replacement of the former Mn^{3+}-rich rows by Co^{3+}-rich rows, without substantial formation of $Co^{3+}_{interlayer}$. Consequently, to explain the observed cation distributions in $S2_{II}$ and $S3_{II}$ it is necessary to conclude that mechanisms 1 and 2 occur in parallel. A structural model for the half super-cell of $S2_{II}$ is drawn in Figure 14 and a schematic description of the type II NaBu-to-$S2_{II}$ transformation presented in Figure 17. The negative layer charge throughout this transformation is compensated by Co^{2+}, Mn^{2+} and H^+ in the interlayer space. The sorption of Co^{2+} as $Co^{2+}_{interlayer}$ is shown explicitly in the reaction scheme because it is the further oxidation of this species, by means of M1 or M2, which is of principal interest. Mn^{2+} and H^+ are essentially ''spectator'' species and may be sorbed at any moment. For the sake of convenience, the sorption of $Mn^{2+}_{interlayer}$ is supposed to occur during the last step of the transformation sequence. Accordingly, intermediate solid phases are artificially enriched in OH groups. The reaction scheme is:

$$Na_{0.333}(Mn^{4+}_{0.667}Mn^{3+}_{0.333})O_2 + 0.44\,H^+ + 0.14\,Co^{2+}$$

$$\xrightarrow[seq1]{\text{M1-step2}} Co^{2+}_{0.055}(Mn^{4+}_{0.722}Mn^{3+}_{0.223}\square_{0.055})O_{1.67}(OH)_{0.33} + 0.055\,Mn^{2+} + 0.085\,Co^{2+} + 0.333\,Na + 0.11\,H^+$$

$$\xrightarrow[seq2]{\text{M1-step3-4}} (Mn^{4+}_{0.722}Mn^{3+}_{0.168}Co^{3+}_{0.055}\square_{0.055})O_{1.56}(OH)_{0.44} + 0.11\,Mn^{2+} + 0.085\,Co^{2+} + 0.333\,Na$$

$$\xrightarrow[seq3]{\text{M2-step1}} Mn^{3+}_{0.055}(Mn^{4+}_{0.722}Mn^{3+}_{0.113}Co^{3+}_{0.055}\square_{0.11})O_{1.56}(OH)_{0.44} + 0.11\,Mn^{2+} + 0.085\,Co^{2+} + 0.333\,Na$$

$$\xrightarrow[seq4]{\text{M1-step2 + M2-step2}} Co^{2+}_{0.017}Mn^{3+}_{0.015}Co^{3+}_{0.04}(Mn^{4+}_{0.722}Mn^{3+}_{0.113}Co^{3+}_{0.055}\square_{0.11})-O_{1.59}(OH)_{0.41} + 0.15\,Mn^{2+} + 0.028\,Co^{2+} + 0.333\,Na + 0.03\,H^+$$

$$\xrightarrow[seq5]{\text{M1-step3-4 + M2-step3}} Mn^{3+}_{0.015}Co^{3+}_{0.023}(Mn^{4+}_{0.722}Mn^{3+}_{0.096}Co^{3+}_{0.089}\square_{0.098})-O_{1.59}(OH)_{0.41} + 0.15\,Mn^{2+} + 0.028\,Co^{2+} + 0.333\,Na + 0.03\,H^+$$

$$\xrightarrow[seq6]{\text{M2-step1}} Mn^{3+}_{0.02}Co^{3+}_{0.023}(Mn^{4+}_{0.722}Mn^{3+}_{0.091}Co^{3+}_{0.089}\square_{0.098})O_{1.59}-(OH)_{0.41} + 0.15\,Mn^{2+} + 0.028\,Co^{2+} + 0.333\,Na + 0.03\,H^+$$

$$\xrightarrow[seq7]{} Mn^{2+}_{0.05}Co^{2+}_{0.028}Mn^{3+}_{0.02}Co^{3+}_{0.023}-(Mn^{4+}_{0.722}Mn^{3+}_{0.091}Co^{3+}_{0.089}\square_{0.098})O_{1.69}(OH)_{0.31} + 0.1\,Mn^{2+} + 0.333\,Na + 0.13\,H^+$$

A detailed analysis of the structural sequence drawn in Figure 17 shows that the degree of freedom of the nature and order of the different chemical reactions, leading to the formation of $S2_{II}$, is relatively limited. This is due to the existence of several strong constraints, which restrict the possibilities at each step of the NaBu-to-CoBi transformation. Among them are (1) the structural formula of initial NaBu crystallites II and the distribution of Mn^{4+}_{layer} and Mn^{3+}_{layer} within these crystallites, (2) the fact that the structural formula for type II CoBi crystallites obtained at the end of the reaction must fit the average chemical composition determined for the whole sample, (3) the avoidance of $\square$-$\square$ pairs at any step of the chemical sequence, and (4) the simultaneous presence of $Co^{2+}_{interlayer}$ and Mn^{3+} in the solid. Indeed, the coexistence of Co^{2+} and Mn^{3+} in $S2_{II}$ may appear surprising because normally the oxidation process continues as long as Mn^{3+} is present. Thus we conclude that $Co^{2+}_{interlayer}$ does not sorb near a layer or interlayer Mn^{3+}, otherwise it would be readily oxidized according to mechanism 1 or 2. The only structural solution is to consider that $Co^{2+}_{interlayer}$ is surrounded by $(Mn^{4+},Co^{3+})_{layer}$ or $(Mn^{2+},Co^{3+})_{interlayer}$. Examination of Figure 17 shows that this stringent requirement is actually fulfilled. Consequently, one merit of this structural model is showing that unoxidized Co^{2+} species must be sorbed later in the structural transformation, when the amount of Mn^{3+} in the solid is sufficiently lowered to allow the formation of Co^{3+}_{layer}-$Co^{2+}_{interlayer}$-Co^{3+}_{layer} or Co^{3+}_{layer}-$Co^{2+}_{interlayer}$-$(Co^{3+}, Mn^{2+}, Co^{2+})_{interlayer}$ sequences along *b*. The probability of a sorbed Co^{2+} species encountering Co^{3+}_{layer}-$\square$-Co^{3+}_{layer} or Co^{3+}_{layer}-$\square$-$(Co^{3+}, Mn^{2+}, Co^{2+})_{interlayer}$ sequences increases with Co loading. This avoidance of Co^{2+}-Mn^{3+} pairs is fully consistent with the observed increase of $Co^{2+}_{interlayer}$ from $\sim$0 ($S1_{II}$) to 0.06 ($S3_{II}$) with increasing Co concentration.

The fact that the number of interlayer cations is greater than the number of vacancies points to the existence of cation pairs across some vacant sites. In birnessite layers, vacant sites result from either the disproportionation reaction (sites 1) or from the migration of Mn^{3+} from layer

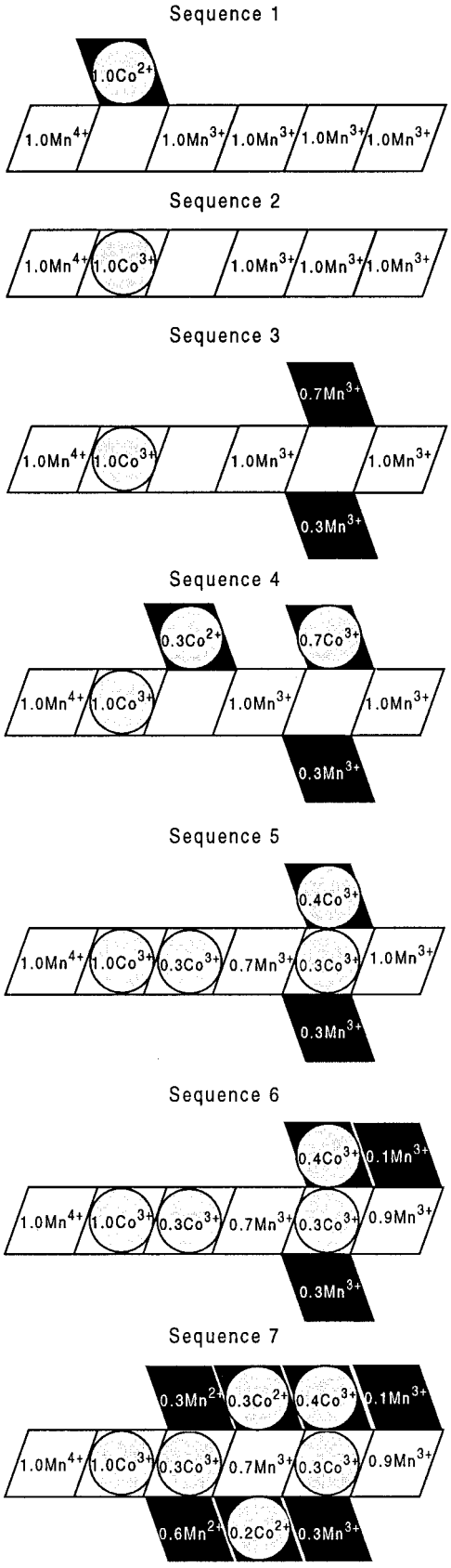

FIGURE 17. Schematic structural representation in the *b-c* plane of the Co^{2+} oxidation to Co^{3+} on type II microcrystallites for S2. Seq. 1–3 = same as in Figure 15; Seq. 4 = sorption of $Co^{2+}_{solution}$ and partial oxidation by $Mn^{3+}_{interlayer}$ according to mechanism M2. Seq. 5 = partial migration of $Co_{interlayer}$ species to layer sites according to mechanisms M1 and M2. Seq. 6 = new migration of Mn^{3+}_{layer} to interlayer site. Seq. 7 = sorption of divalent species. This suite of chemical reactions obeys the following crystal chemical conditions: (1) The oxidation of Co and the acidic weathering of NaBu occur simultaneously; (2) Sorbed Co^{2+} is oxidized by nearest Mn^{3+} (i.e., absence of $Co^{2+}_{interlayer}$-Mn^{3+}_{layer} pairs); and (3) avoidance of Mn^{3+}_{layer}-Co^{3+}_{layer}-Mn^{3+}_{layer} and □-□ sequences. The sorption of $Mn^{2+}_{solution}$ is not temporally constrained, with the entire amount of $Mn^{2+}_{interlayer}$ arbitrarily sorbed at the end of the oxidation sequence.

→

to interlayer positions (site 2). Interlayer cations compensate the layer charge deficiency created by the absence of Mn^{4+}_{layer}. For electrostatic reasons it is unlikely that $Mn^{2+}_{solution}$ sorbs on site 2 (opposite an Mn^{3+} or Co^{3+}) because this would form $(Mn,Co)^{3+}_{interlayer}$-□-$Mn^{2+}_{interlayer}$ pairs across vacancies, and therefore cause an excess of charge. For this reason, it is most likely that $Mn^{2+}_{solution}$ sorbs on site 1, as would $Co^{2+}_{interlayer}$ (Figs. 14 and 17). In Figure 14, these sites correspond to positions with an occupancy greater than one.

***S3*$_{II}$.** *S3*$_{II}$ microcrystallites contain large amounts of Co^{3+}_{layer} (0.12) and $Co^{2+}_{interlayer}$ (0.06) as well as some $Co^{3+}_{interlayer}$ (0.03) and $Mn^{3+}_{interlayer}$ (0.01). The scarcity of $Mn^{3+}_{interlayer}$ in $S3_{II}$ compared with HBi (0.11) can be explained by its reduction to Mn^{2+} species because of the large concentration of $Co^{2+}_{solution}$ (2×10^{-2} M, Table 1). This sample has more interlayer cations (0.13) than layer vacancies (0.10), and this excess of interlayer cations points to the presence of pairs of TC-sharing cations across vacancies [$(Mn,Co)^{2+}_{interlayer}$-□-$(Mn,Co)^{2+}_{interlayer}$] as for $S2_{II}$. Interlayer cations, together with OH groups, compensate the deficiency of layer cationic charge originating from heteroionic substitutions and lattice vacancies. The increased amount of interlayer species relative to vacant sites is fully consistent with the lowering of OH groups from 0.32 ($S1_{II}$) to 0.28 ($S3_{II}$).

A realistic structural model of the layer structure for microcrystallites type II is drawn in Figure 14, and a schematic description of the type II NaBu to $S3_{II}$ transformation is shown in Figure 18. The structural formula obtained for these crystallites II is in good agreement with the average chemical composition of the bulk sample.

The structures of Co-rich asbolane and Co-rich lithiophorite revisited

The results obtained for the synthetic CoBi samples shed light on the immobilization mechanism of Co in natural asbolane and lithiophorite. Figure 6 shows that RSFs for natural samples and S1 and S2 bear a strong resemblance. Consequently, the increase in intensity of

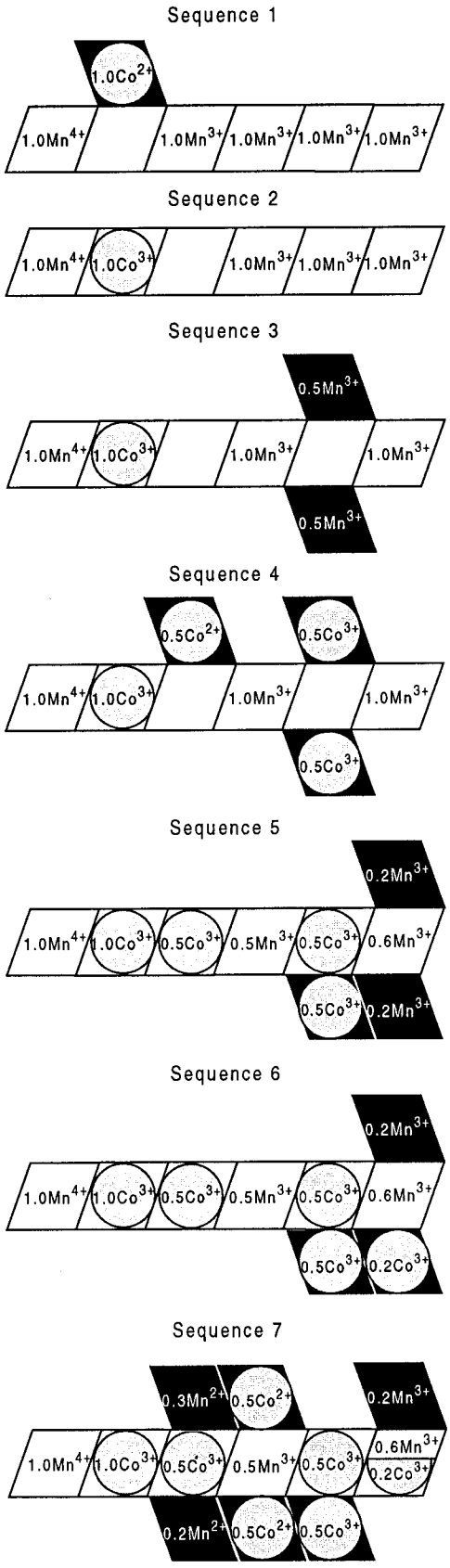

FIGURE 18. Schematic structural representation in the *b-c* plane of the Co^{2+} oxidation to Co^{3+} on type II microcrystallites for S3. Seq. 1–5: same as in Figure 18; Seq. 6 = new sorption and oxidation of $Co^{2+}_{solution}$ by $Mn^{3+}_{interlayer}$ according to mechanism M2. Seq. 7 = migration of $Co^{3+}_{interlayer}$ and sorption of divalent species.
←

the Co-O and Co-Mn_1 RSF peaks relative to Mn-O and Mn-Mn_1 in natural samples is fully accounted for by the structural Co^{2+}-to-Co^{3+} oxidation mechanism proposed for birnessite. This startling enhancement of Co-RSF peaks was noted by Manceau et al. (1987), but they failed at that time to determine whether Co was precipitated as CoOOH or segregated or substituted for Mn in the phyllomanganate layers. The evidence supporting the lattice migration of Co^{3+} (Fig. 14) answers this important geochemical question and provides an atomic-scale explanation of the weak extractability of Co once sorbed onto natural manganese oxides (McKenzie 1967). In addition, the precipitation of a discrete CoOOH phase in natural samples can be readily dismissed, from the comparison with EXAFS spectra (Fig. 5, top).

The close similarity of Mn RSFs for natural, HBi, and Co-sorbed samples also provides insight into the layer structure of natural phyllomanganates. Figure 6 shows that Mn-O and Mn-nearest Mn peaks for natural samples and S2 have similar intensities (~8) on the vertical scale. This amplitude is significantly lower than that of stoichiometric λ-MnO_2 (~10, Fig. 7), which suggests that natural samples contain heterovalent Mn atoms and layer vacancies, as is generally the case for synthetic phyllomanganates (Strobel et al. 1987). The existence of lattice vacancies in natural samples is also supported by the presence of a third peak in the Co and Mn RSFs (TC linkages) and by the general similarity of the local Co environment in natural, S1, and S2 samples. A noticeable difference between natural and synthetic samples is the relatively low intensity of the third RSF peaks in the former. This result indicates that the majority, if not all, of the Co atoms migrated to vacancy sites following oxidation to Co^{3+}. The small amount of TC linkages can be attributed to the sorption of some divalent metal species (e.g., Mn^{2+}) near Co^{3+}_{layer} positions.

Evidence for the oxidation of Co^{2+} by Mn^{3+}

We assumed in the preceding discussion that Co^{2+} is oxidized exclusively by Mn^{3+} in the HBi structure. Similar conclusions have been made by Hem et al. (1985) in their study of CoOOH coprecipitation with manganese oxides under oxygen. This conclusion, however, appears to contradict the findings of Crowther et al. (1983), who identified Mn^{4+} as the dominant electron sink in the oxidation of Co^{2+} by birnessite, using an XPS technique. Although there are some differences in the solution chemical conditions used in the present study compared with Crowther et al. (1983), further justification of our position

is warranted. The relative oxidizing strengths of Mn^{3+} and Mn^{4+} in a mixed-valency oxide can be inferred from the thermodynamic data of stoichiometric Mn^{3+} and Mn^{4+} oxides. Figure 19 shows a simplified thermodynamic stability diagram in which the phase boundaries of β-MnO_2 and γ-MnOOH (as representative Mn^{4+} and Mn^{3+} oxides) with $Mn^{2+}_{(aq)}$ ($a^{2+}_{Mn} = 10^{-6}$ M) are plotted. Thermodynamic data for the calculation of these phase boundaries was obtained from Bard et al. (1985), whereas the Mn^{2+} activity was chosen in accordance with the initial experimental conditions. The stability boundaries of α-MnOOH and Mn_2O_3 with Mn^{2+} plot in a similar region to that for γ-MnOOH, so that the position shown for γ-MnOOH can be considered as representative of the ''family'' of Mn^{3+} oxides. It should be noted that under acidic condition Mn^{3+} oxides are unstable with respect to disproportionation to MnO_2 and Mn^{2+}, however good evidence exists for the metastability of Mn^{3+} oxides and Mn^{4+}-Mn^{3+} mixed-valency oxides under mildly acidic conditions (Giovanoli and Leuenberger 1969; Giovanoli et al. 1970; Hem 1980; Silvester et al. 1997). As observed from Figure 19 γ-MnOOH is a stronger oxidant than the pure Mn^{4+} β-MnO_2 phase for pH conditions below 7, while for pH conditions above 7, the opposite is true. The relative oxidizing strengths of γ-MnOOH and β-MnO_2 at low pH have been demonstrated in the case of Cr^{3+} oxidation by γ-MnOOH (Johnston and Xyla 1991) in which the rate of Cr^{3+} oxidation at pH 4 is several orders of magnitude faster than that by β-MnO_2 (Eary and Rai 1987). Similarly, the rate of Cr^{3+} oxidation by HBi at pH 4 is also very high (Silvester et al. 1995). This latter observation demonstrates that, in terms of the oxidizing strength, HBi is more analogous to an Mn^{3+} oxide than an Mn^{4+} oxide. The relative positions of the γ-MnOOH and β-MnO_2 phase boundaries with Mn^{2+}, shown in Figure 19, are also supported by studies of the oxidation of $Co^{2+}EDTA^{2-}$ (EDTA = ethylenediaminetetraacetic acid) to $Co^{3+}EDTA^{-}$ at the surface of β-MnO_2 (Jardine and Taylor 1995). These authors concluded that at pH 7 β-MnO_2 is a more likely electron sink, although they noted that both β-MnO_2 and γ-MnOOH should have similar oxidizing strengths at this solution pH.

The redox level for the Co^{2+}-CoBi couple is not known. The situation is complicated further by the existence of both $Co^{3+}_{interlayer}$ and Co^{3+}_{layer} in CoBi, the proportions of which depend on the Co loading. Again it is necessary to compare CoBi with a stoichiometric Co^{3+} oxide phase to assess the feasibility of Co^{2+} oxidation by Mn^{3+} or Mn^{4+}. To this end, the redox level of the heterogenite CoOOH-Co^{2+} couple is plotted in Figure 19. For the free energy of formation of heterogenite, we used the data calculated by Hem et al (1985). The stability boundary of CoOOH with Co^{2+} has been plotted at $a^{2+}_{Co} = 10^{-3}$ M, representative of the initial reaction conditions upon addition of Co^{2+} to an NaBu suspension. Comparison of the CoOOH-Co^{2+} boundary with that for γ-MnOOH-Mn^{2+} shows that the reaction is thermodynamically favorable, leading to the oxidation of Co^{2+} and the reduction of

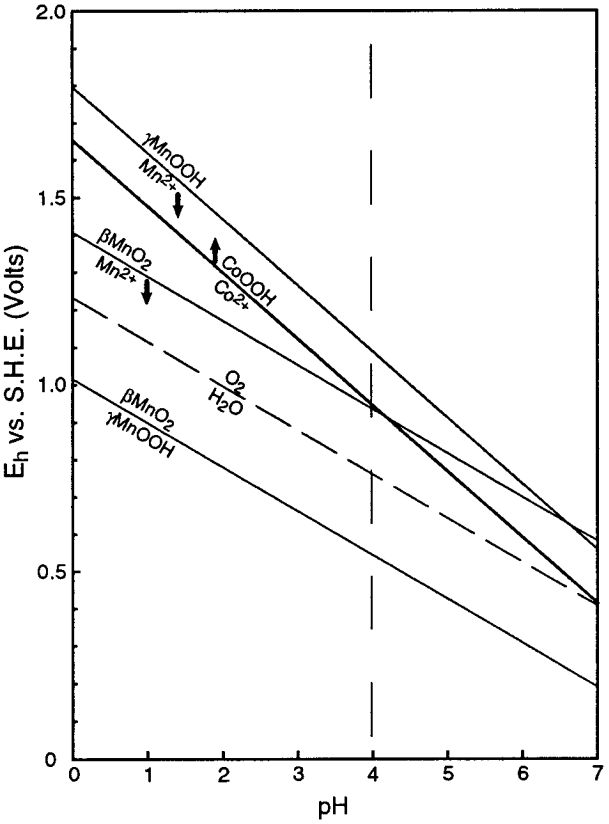

FIGURE 19. Eh-pH diagram showing the stability boundaries of γ-MnOOH and β-MnO_2 with Mn^{2+} ($a^{2+}_{Mn} = 10^{-6}$ M). Also shown are the stability boundaries between CoOOH and Co^{2+} ($a^{2+}_{Co} = 10^{-3}$ M), β-MnO_2 and γ-MnOOH, and H_2O and O_2. Arrows refer to the movement of stability boundaries upon reaction between γ-MnOOH or β-MnO_2 and Co^{2+}.

γ-MnOOH. As the reaction proceeds the stability boundaries move in the direction shown by the arrows, tending toward equilibrium. Comparison of the β-MnO_2-Mn^{2+} boundary with CoOOH-Co^{2+} shows that the reaction is unfavorable below pH 4.5, with any reaction between Co^{2+} and β-MnO_2 leading to the further separation of the stability boundaries. As a result it is clear that an Mn^{3+} oxide is a stronger oxidant for Co^{2+} for all pH conditions less than ~7. Because the CoBi samples in this study were prepared at pH 4, it is reasonable to conclude that the most likely electron sink for the oxidation of Co^{2+} to Co^{3+} is Mn^{3+} in HBi.

An additional factor favoring of Mn^{3+} as the prime oxidant for Co^{2+} is the complementary nature of the electron transfer according to:

$$Mn^{3+} + Co^{2+} \rightarrow Mn^{2+} + Co^{3+}.$$

The same is not true for Co^{2+} oxidation by Mn^{4+}, in which it is necessary to invoke the presence of an Mn^{3+} oxide as a reaction product or intermediate. The very low redox level of the β-MnO_2–γ-MnOOH couple shown in

Figure 19 demonstrates that this is probably the least likely pathway for Co^{2+} oxidation.

In addition to the thermodynamic arguments in favor of Mn^{3+} as the electron sink in HBi, supporting evidence is found in the EXAFS analysis, in particular the observed increase in $CN_{Mn\text{-}O}$ with increased Co loading (Fig. 7). In HBi the intensity of this peak is significantly reduced compared with that for the stoichiometric Mn^{4+} oxide λ-MnO_2, because of the presence of both Mn^{4+} and Mn^{3+} in the structure. The effect of Mn^{3+} on the intensity of the peaks in the Mn RSF can be observed in the RSF of γ-MnOOH (Fig. 7) and can be attributed to the distribution of Mn-O and Mn-Mn distances resulting from Jahn-Teller distortion of the $Mn^{3+}O_6$ octahedron. A mechanism of Co^{2+} oxidation involving Mn^{3+} would result in a decrease in the Mn^{3+} content with increased Co loading, and in turn to the augmentation of the Mn-O peak in the RSF, as observed. Consequently, the increase in amplitude of the Mn-O peak with increased Co loading strongly supports the oxidation of Co^{2+} by Mn^{3+}.

Acknowledgments

Alain Plançon is acknowledged for making available his X-ray simulation software and LURE laboratory for providing access to the beam.

References cited

Balistrieri, L.S. and Murray, J.W. (1986) The surface chemistry of sediments from the Panama Basin: The influence of Mn oxides on metal adsorption. Geochimica et Cosmochimica Acta, 50, 2235–2243.

Bard, A.J., Parsons, R., and Jordan, J. (1985) Standard potentials in aqueous solution, 834 p. Marcel Dekker, New York.

Bidoglio, G., Gibson, P.N., O'Gorman, M., and Roberts, K.J. (1993) X-ray absorption spectroscopy investigation of surface redox transformations of thallium and chromium on colloidal mineral oxides. Geochimica et Cosmochimica Acta, 57, 2389–2394.

Brouder, C. (1990) Angular dependence of X-ray absorption spectra. Journal of Physics: Condensed Matter, 2, 701–738.

Burns, R.G. and Burns, V.M. (1977) The mineralogy and crystal chemistry of deep-sea manganese nodules—a polymetallic resource of the twenty-first century. Philosophical Transaction of the Royal Society of London, A286, 283–301.

Christensen, A.N. (1965) A single crystal X-ray diffraction study of $Mn(OH)_2$. Acta Chemica Scandinavica, 19, 1765–1766.

Chukhrov, F.V., Gorshkov, A.I., Vitovskaya, I.V., Drits, V.A., Sivtsov, A.I., and Dikov, Y.P. (1980) Crystallochemical nature of Co-Ni asbolan. AN SSSR Izvestiya, Seriya Geologicheskaya, 6, 73–81. (Translated in International Geological Review, 24, 598–604, 1982).

Chukhrov, F.V., Gorshkov, A.I., Drits, V.A., Sivtsov, A.I., and Dikov, Y.P. (1982) New structural variety of asbolite. Investiya Akademie Nauk, SSSR, Seriya Geologicheskaya, 6, 69–77.

Chukhrov, F.V., Sakharov, B.A., Gorshkov, A.I., Drits, V.A., and Dikov, Y.P. (1985) Crystal structure of birnessite from the Pacific Ocean. International Geology Review, 1985, 27, 1082–1088 (translated from Investia Akademie Nauk, SSSR, Seriya Geologicheskaya, 8, 66–73).

Chukhrov, F.V., Gorshkov, A.I., and Drits, V.A. (1989) Supergenic manganese hydrous oxides, 208 p. Nauka, Moscow.

Crowther, D.L., Dillard, J.G., and Murray, J.G. (1983) The mechanism of Co(II) oxidation on synthetic birnessite. Geochimica et Cosmochimica Acta, 47, 1399–1403.

Delaplane, R.G., Ibers, J.A., J.R., F., and J.J., R. (1969) Structure of CoOOH. Journal of Chemical Physics, 50, 1920–1925.

Dillard, J.G., Crowther, D.L., and Murray, J.W. (1982) The oxidation states of cobalt and selected metals in Pacific ferromanganese nodules. Geochimica et Cosmochimica Acta, 46, 755–759.

Drits, V.A. and Tchoubar, C. (1990) X-ray diffraction by disordered lamellar structures: Theory and applications to microdivided silicates and carbons, 371 p. Springer Verlag, Berlin.

Drits, V.A., Silvester, E., Gorshkov, A.I., and Manceau, A. (1997) Structure of synthetic monoclinic Na-rich birnessite and hexagonal birnessite: I. Results from X-ray diffraction and selected-area electron diffraction. American Mineralogist, 82, 946–961.

Eary, L.E. and Rai, D. (1987) Kinetics of chromium(III) oxidation to chromium(VI) by reaction with manganese dioxide. Environmental Science and Technology, 21, 1187–1193.

Fendorf, S.E. and Zasoski, R.J. (1992) Chromium(III) oxidation by δ-MnO2: Characterization. Environmental Science and Technology, 26, 79–85.

Fendorf, S.E., Zasoski, R.J., and Burau, R. (1993) Competing metal ion influences on chromium(III) oxidation by birnessite. Soil Science Society of America Journal, 57, 1508–1515.

Friedl, G., Wehrli, B., and Manceau, A. (1997) Solid phases in the cycling of manganese in eutrophic lakes. New insights from EXAFS spectroscopy. Geochimica et Cosmochimica Acta, 61, 275–290.

Giovanoli, R. and Leuenberger, U. (1969) Über die Oxydation von Manganoxidhydroxid. Helvetica Chimica Acta, 52, 2333–2347.

Giovanoli, R., Stähli, E., and Feitknecht, W. (1970) über Oxidhydroxide des vierwertigen Mangans mit Schichtengitter: 1. Mitteilung: Natrium-mangan(II,III)manganat(IV). Helvetica Chimica Acta, 53, 454–464.

Glasser, L.S.D. and Ingram, L. (1968) Refinement of the crystal structure of groutite, α-MnOOH. Acta Crystallographica, B24, 1233–1236.

Gray, M.J. and Malati, M.A. (1979) Adsorption from aqueous solution by δ-manganese dioxide: II. Adsorption of some heavy metal cations. Journal of Chemical Technology and Biotechnology, 29, 135–144.

Hazemann, J.L., Manceau, A., Sainctavit, P., and Malgrange, C. (1992) Structure of the αFe_xAl_{1-x}OOH solid solution: I. Evidence by polarized EXAFS for an epitaxial growth of hematite-like clusters in diaspore. Physics and Chemistry of Minerals, 19, 25–38.

Heald, S.M. and Stern, E.A. (1977) Anisotropic x-ray absorption in layered compounds. Physical Review, B16, 5549–5559.

Hem, J.D. (1980) Redox coprecipitation mechanisms of manganese oxides. In M.C. Kavanaugh and J.O. Leckie, Eds., Particulates in water, 189, p. 45–72. American Chemical Society, Washington, D.C.

Hem, J.D., Roberson, C.E., and Lind, C.J. (1985) Thermodynamic stability of CoOOH and its coprecipitation with manganese. Geochimica et Cosmochimica Acta, 49, 801–810.

Jardine, P.M. and Taylor, D.L. (1995) Kinetics and mechanisms of Co(II)EDTA oxidation by pyrolusite. Geochimica et Cosmochimica Acta, 59, 4193–4203.

Johnston, C.A. and Xyla, A.G. (1991) The oxidation of chromium(III) to chromium(VI) on the surface of manganite (γ-MnOOH). Geochimica et Cosmochimica Acta, 55, 2861–2866.

Kuma, K., Usui, A., Paplawsky, W., Gedulin, B., and Arrhenius, G. (1994) Crystal structures of synthetic 7 Å and 10 Å manganates substituted by mono- and divalent cations. Mineralogical Magazine, 58, 425–447.

Llorca, S. (1987) Nouvelles donnees sur la composition et la structure des lithiophorites, d'après des échantillons de Nouvelle-Calédonie. Comptes Rendus de l'Académie des Sciences de Paris, 304, 1518–1520.

Loganathan, P. and Burau, R.G. (1973) Sorption of heavy metal ions by hydrous manganese oxide. Geochimica et Cosmochimica Acta, 37, 1277–1293.

Manceau, A. (1995) The mechanism of anion adsorption on Fe oxides: Evidence for the bonding of arsenate tetrahedra on free $Fe(O,OH)_6$ edges. Geochimica et Cosmochimica Acta, 59, 3647–3653.

Manceau, A. and Charlet, L. (1992) X-ray absorption spectroscopic study of the sorption of Cr(III) at the oxide/water interface: I. Molecular mechanism of Cr(III) oxidation on Mn oxides. Journal of Colloid and Interface Science, 148, 443–458.

Manceau, A. and Combes, J.M. (1988) Structure of Mn and Fe oxides and oxyhydroxides: a topological approach by EXAFS. Physics and Chemistry of Minerals, 15, 283–295.

Manceau, A. and Gates, W. (1997) Surface structural model for ferrihydrite. Clays and Clay Minerals, in press.

Manceau, A., Llorca, S., and Calas, G. (1987) Crystal chemistry of cobalt and nickel in lithiophorite and asbolane from New Caledonia. Geochimica et Cosmochimica Acta, 51, 105–113.

Manceau, A., Bonnin, D., Kaiser, P., and Frétigny, C. (1988) Polarized EXAFS of biotite and chlorite. Physics and Chemistry of Minerals, 16, 180–185.

Manceau, A., Bonnin, D., Stone, W.E.E., and Sanz, J. (1990) Distribution of Fe in the octahedral sheet of trioctahedral micas by polarized EXAFS. Comparison with NMR results. Physics and Chemistry of Minerals, 17, 363–370.

Manceau, A., Gorshkov, A.I., and Drits, V.A. (1992) Structural chemistry of Mn, Fe, Co, and Ni in Mn hydrous oxides: Part II. Information from EXAFS spectroscopy and electron and X-ray diffraction. American Mineralogist, 77, 1144–1157.

McKenzie, R.M. (1967) The sorption of cobalt by manganese minerals in soils. Australian Journal of Soil Research, 5, 235–246.

——— (1970) The reaction of cobalt with manganese dioxide minerals. Australian Journal of Soil Research, 8, 97–106.

——— (1980) The adsorption of lead and other heavy metals on oxides of manganese and iron. Australian Journal of Soil Research, 18, 61–73.

Means, J.L., Crerar, D.A., Borcsilk, M.P., and Duguid, J.O. (1978) Adsorption of Co and selected actinides by Mn and Fe oxide in soils and sediments. Geochimica et Cosmochimica Acta, 42, 1763–1773.

Murray, J.W. (1975) The interaction of cobalt with hydrous manganese dioxide. Geochimica et Cosmochimica Acta, 39, 635–647.

Murray, J.W. and Dillard, J.G. (1979) The oxidation of cobalt(II) adsorbed on manganese dioxide. Geochimica et Cosmochimica Acta, 43, 781–787.

Oscarson, D.W., Huang, P.M., Liaw, W.K., and Hammer, U.T. (1983) Kinetics of oxidation of arsenite by various manganese dioxides. Soil Science Society of America Journal, 47, 644–648.

Ostwald, J. (1984) Two varieties of lithiophorite in some Australian deposits. Mineral Magazine, 48, 383–388.

Plançon, A. (1981) Diffraction by layer structure containing different kinds of layers and stacking faults. Journal of Applied Crystallography, 14, 300–304.

Post, J.E. and Appleman, D.E. (1988) Chalcophanite, $ZnMn_3O_7 \cdot 3H_2O$: New crystal-structure determination. American Mineralogist, 73, 1401–1404.

Post, J.E. and Veblen, D.R. (1990) Crystal structure determinations of synthetic sodium, magnesium, and potassium birnessite using TEM and the Rietveld method. American Mineralogist, 75, 477–489.

Reynolds, R.C. Jr. (1989) Diffraction by small and disordered crystals. In Mineralogical Society of America Reviews in Mineralogy, 6, 145–181.

Sakharov, B.A., Naumov, A.S., and Drits, V.A. (1982a) X-ray diffraction by mixed-layer structures with random distribution of stacking faults. Døklady Akademie Nauk SSSR, 265, 339–343.

——— (1982b) X-ray intensities scattered by layer structure with short range ordering parameters S=1 and G=1. Døklady Akademie Nauk SSSR, 265, 871–874.

Silvester, E., Charlet, L., and Manceau, A. (1995) The mechanism of chromium(III) oxidation by Na-buserite. Journal of Physical Chemistry, 99, 16662–16772.

Silvester, E., Manceau, A., and Drits, V.A. (1997) Structure of sythetic monoclinic Na-rich birnessite and hexagonal birnessite: II. Results from chemical studies and EXAFS spectroscopy. American Mineralogist, 82, 962–978.

Stern, E.A. and Kim, K. (1981) Thickness effect on the extended x-ray absorption fine structure amplitude. Physical Review, 23, 3781–3787.

Stone, A.T. and Morgan, J.J. (1984) Reduction and dissolution of manganese(III) and manganese(IV) oxides by organics. 2. Survey of the reactivity of organics. Environmental Science and Technology, 18, 617–624.

Stone, A.T. and Ulrich, H.J. (1989) Kinetics and reaction stoichiometry in the reductive dissolution of manganese(IV) dioxide and Co(III) oxide by hydroquinone. Journal of Colloid and Interface Science, 132, 509–522.

Strobel, P., Charenton, J.C., and Lenglet, M. (1987) Structural chemistry of phyllomanganates: Experimental evidence and structural models. Revue de Chimie Minérale, 24, 199–220.

Taylor, R.M. (1968) The association of manganese and cobalt in soils—further observations. Journal of Soil Science, 19, 77–80.

Taylor, R.M. and McKenzie, R.M. (1966) The association of trace elements with manganese minerals in Australian soils. Australian Journal of Soil Research, 4, 29–39.

Taylor, R.M., McKenzie, R.M., and Norrish, K. (1964) The mineralogy and chemistry of manganese in some Australian soils. Australian Journal of Soil Research, 2, 235–248.

Teo, B.K. (1986) EXAFS: Basic principles and data analysis, 349 p. Springer-Verlag, Berlin.

Thackeray, M.M., de Kock, A., and David, W.I.F. (1993) Synthesis and structural characterisation of defect spinels in the lithium-manganese-oxide system. Material Research Bulletin, 28, 1041–1049.

Traina, S.J. and Doner, H.E. (1985) Heavy metal induced releases of manganese(II) from a hydrous manganese dioxide. Soil Science Society of America Journal, 49, 317–321.

Wadsley, A.D. (1955) The crystal structure of chalcophanite, $ZnMn_3O_7 \cdot 3H_2O$. Acta Crystallographica, 8, 1165–172.

Manuscript received February 3, 1997
Manuscript accepted July 23, 1997